Stockholm University

Going for gold

A spectroelectrochemical and catalytic study of gold materials

Sara Boscolo Bibi

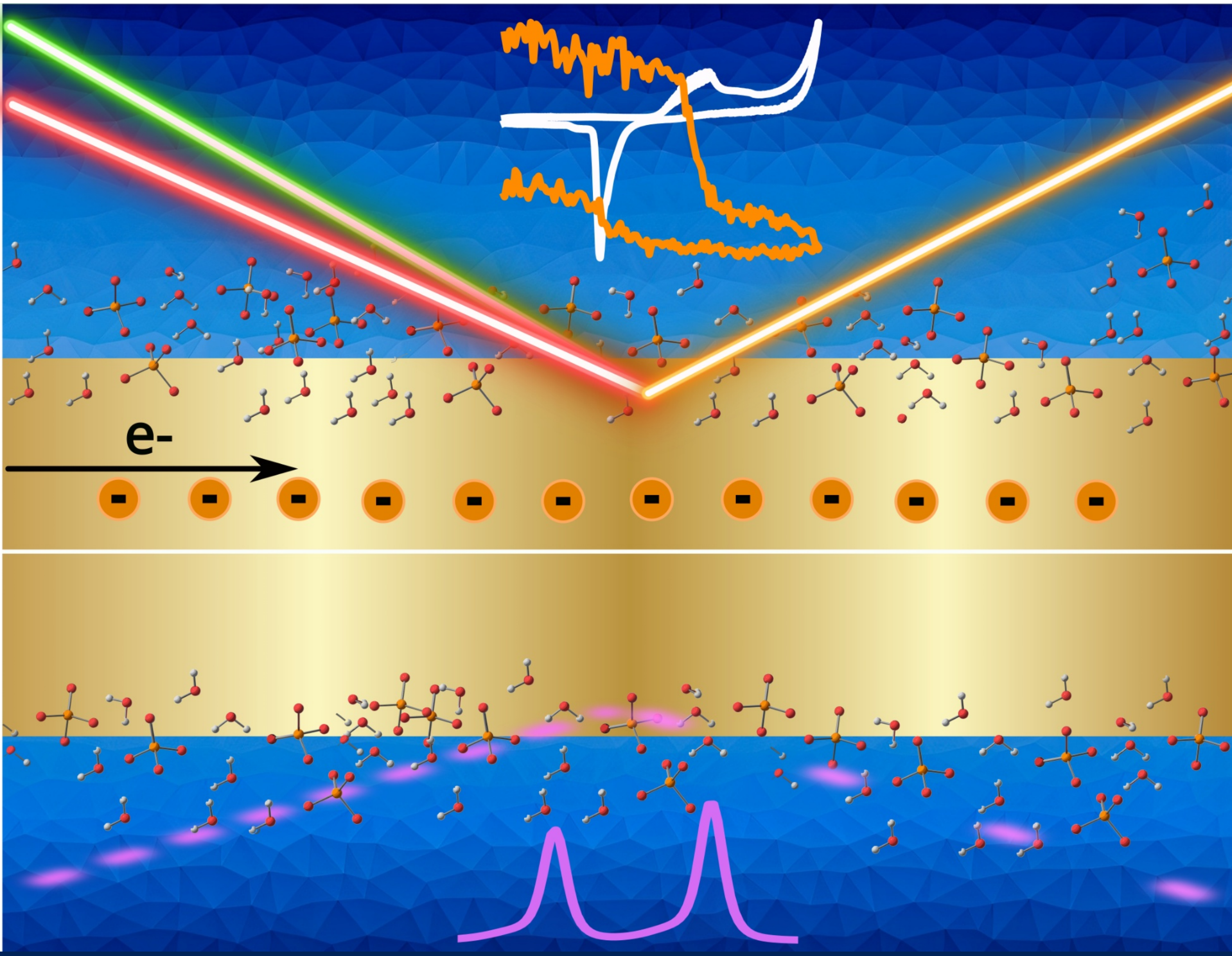

Doctoral Thesis in Chemical Physics at Stockholm University, Sweden 2024

Going for gold

A spectroelectrochemical and catalytic study of gold materials

Sara Boscolo Bibi

Academic dissertation for the Degree of Doctor of Philosophy in Chemical Physics at Stockholm University to be publicly defended on Friday 26 January 2024 at 13.00 in sal FR4, AlbaNova universitetscentrum, Roslagstullsbacken 21.

Abstract

With the increase in demand for renewable energy, understanding chemical processes is essential for improving the design of catalysts in order to achieve better performance. This thesis summarises the experimental investigation of three types of catalytic gold materials: gold oxide formed from gold films, oxide-derived gold (OD-Au) produced from gold films, and gold nanoparticles supported on metal oxides. Different spectroscopic techniques were employed, such as *operando* sum frequency generation (SFG) and *in situ* and *ex situ* X-ray spectroscopies. These methods allowed the probing of the electronic and chemical states of gold after oxidising electrochemical treatments. The results indicate the presence of subsurface gold oxide remnants after formation of OD-Au, which may help explain its improved catalytic properties with respect to pure gold. In addition, a mathematical model to couple the early stages of gold oxide formation with the nonlinear optical response of gold during this process is presented. This model suggests that the growth proceeds from small oxide islands to 3D oxide growth, while SFG oxidation variation is due to the suppression of the free electron density by negatively-charged adsorbing oxygen atoms. Gold oxide was also studied with both *in situ* and *operando* X-ray spectroscopies, showing the importance of a continuous electrochemical treatment during measurements to avoid beam induced effects. Furthermore, gold nanoparticles supported on metal oxides (TiO_2 and γ-Fe_2O_3) were investigated mainly with mass spectrometry. The results indicate two different reaction pathways for oxidation of CO to CO_2 depending on the type of metal oxide support. These findings could be used to help design future gold-based catalysts.

Keywords: *Gold oxidation, oxide-derived metals, electrochemistry, X-ray spectroscopy, optical nonlinear spectroscopy, AuNPs supported in metal oxides, mass spectrometry.*

Stockholm 2023
http://urn.kb.se/resolve?urn=urn:nbn:se:su:diva-224357

ISBN 978-91-8014-615-9
ISBN 978-91-8014-616-6

Stockholm University

Department of Physics

Stockholm University, 106 91 Stockholm

GOING FOR GOLD

Sara Boscolo Bibi

Stockholm
University

Going for gold

A spectroelectrochemical and catalytic study of gold materials

Sara Boscolo Bibi

©Sara Boscolo Bibi, Stockholm University 2024

ISBN print 978-91-8014-615-9
ISBN PDF 978-91-8014-616-6

Printed in Sweden by Universitetsservice US-AB, Stockholm 2023

Ai miei genitori

La chimica è una cosa che serve a tutto.
Serve a coltivarsi, serve a crescere,
serve a inserirsi in qualche modo nelle cose concrete.

Primo Levi (1919 - 1987)

Contents

List of Papers iii

Author's contribution v

Abbreviations vii

List of Figures ix

1 Introduction 1
- 1.1 Surface chemistry 1
  - 1.1.1 Electrochemical processes at the interface 3
- 1.2 Properties of gold 6
  - 1.2.1 The d-band model 6
  - 1.2.2 Electrochemistry of gold 8
  - 1.2.3 Gold as a catalyst 11
- 1.3 This thesis 13

2 Methods 15
- 2.1 Spectroscopic techniques 15
  - 2.1.1 Optical sum frequency generation spectroscopy 15
  - 2.1.2 X-ray photoelectron spectroscopy 18
  - 2.1.3 X-ray absorption spectroscopy 21
- 2.2 Light sources and detection systems 23
  - 2.2.1 Optical set-up 23
  - 2.2.2 X-ray generation: synchrotron radiation 26
  - 2.2.3 POLARIS system for HP-XPS at beamline P22 27
  - 2.2.4 von Hamos-type geometry spectrometer for HERFD-XANES at beamline P64 28
- 2.3 Electrochemical characterisation 29
  - 2.3.1 Electroanalytical chemistry 29
  - 2.3.2 Electrochemical cell for SFG spectroscopy 32
  - 2.3.3 Electrochemical cells for X-ray spectroscopies 33
  - 2.3.4 Preparation of gold electrodes for spectroelectrochemical measurements 35
  - 2.3.5 Calibration of the gold reference electrode 35

2.4 Mass spectrometry 36

3 Summary of results **39**

3.1 Study of electrochemically-formed oxide-derived gold from gold films 39

3.2 Models for electro-oxidation and nonlinear optical response of gold surfaces 45

3.3 *In situ* investigation of electrochemically-formed gold oxide from gold films with X-ray spectroscopies 49

3.4 Catalytic studies of low-temperature CO oxidation on Au-Fe_2O_3 and Au-TiO_2 54

4 Conclusions and Outlook **59**

Populärvetenskaplig sammanfattning **lxi**

Acknowledgements **lxiii**

References **lxv**

List of Papers

The following papers, referred to in the text by their Roman numerals, are included in this thesis.

PAPER I: **Multi-spectroscopy study of electrochemically-formed oxide-derived gold electrodes**
Sara Boscolo Bibi, Ahmed M. El-Zohry, Bernadette Davies, Vladimir Grigorev, Christopher M. Goodwin, Patrick Lömker, Alexander Holm, Harri Ali-Löytty, Fernando Garcia-Martinez, Christoph Schlueter, Markus Soldemo, Sergey Koroidov, and Tony Hansson
Accepted in PCCP

PAPER II: **Electro-oxidation and nonlinear optical response of a gold surface**
Sara Boscolo Bibi, Ahmed M. El-Zohry, Sergey Koroidov, and Tony Hansson
Manuscript

PAPER III: **X-ray spectroscopy study of electrochemically oxidized gold**
Sara Boscolo Bibi, Fernando Garcia-Martinez, Bernadette Davies, Vladimir Grigorev, Patrick Lömker, Aleksandr Kalinko, Christoph Schlueter, Tony Hansson, Markus Soldemo, and Sergey Koroidov
Manuscript

PAPER IV: **A water–promoted Mars–van–Krevelen reaction dominates low–temperature CO oxidation over Au–Fe_2O_3, but not over Au–TiO_2**
Alexander Holm, Bernadette Davies, Sara Boscolo Bibi, Felix Santiago Moncada Arias, Joakim Halldin-Stenlid, Laurynas Paskevicius, Vincent Claman, Adam Slabon, Cheuk-Wai Tai, Egon Campos dos-Santos, and Sergey Koroidov
Submitted

Full article and figure reprints were made with permission from publishers under the CC BY-NC 3.0 Deed license.

Author's contribution

The scientific research work presented in this thesis is the result of a group effort in each single step of the overall working process.

PAPER I: My contribution was to design the electrochemical cell, to commission the gold sample for SFG measurements, to conduct the SFG experiments and data analysis, to plan the XPS data acquisition during the beamtime and analysis of that data, and writing the manuscript.

PAPER II: My contribution was to conduct the SFG experiments and data analysis, to perform some initial numerical calculations, and was actively involved in the planning, theoretical discussion, and writing of the manuscript.

PAPER III: My contribution was to commission the gold sample for XPS measurements, to plan the XPS data acquisition during the beamtime and its data analysis, performed the HERFD-XANES linear fit and analysis, and writing the manuscript.

PAPER IV: My contribution was to be involved in the characterisation and data analysis, and was involved in the proofreading and editing of the manuscript.

Parts of the text and some images from chapters 1 and 2 are taken from the licentiate thesis.[1] Additional text was also written in these sections exclusively for this thesis.

Abbreviations

BE	Binding energy
BBO	Beta-barium borate
CA	Chronoamperometry
CCD	Charge coupled device
CE	Counter electrode
CT	Charge transport
CV	Cyclic voltammetry
CW	Continuous wave
DFT	Density functional theory
EC	Electrochemical cell
EDL	Electric double layer
ESCA	Electron spectroscopy for chemical analysis
EXAFS	Extended X-ray absorption fine structure
FWHM	Full width at half maximum
HER	Hydrogen evolution reaction
HERFD	High-energy resolution fluorescence detected
HOMO	Highest occupied molecular orbital
HP-XPS	High-pressure X-ray photoelectron spectroscopy
ICP	Inductively coupled plasma
IHP	Inner Helmholtz plane
IMFP	Inelastic mean free path
IR	Infrared
KE	Kinetic energy
LH	Langmuir-Hinshelwood mechanism
LUMO	Lowest unoccupied molecular orbital
MS	Mass spectrometry
n-DFG	Non-collinear difference-frequency generator
NEXAFS	Near-edge X-ray absorption fine structure
NP	Nanoparticle
OER	Oxygen evolution reaction
OHP	Outer Helmholtz plane
PICS	Photoionization cross section
QRE	Quasi reference electrode
RE	Reference electrode
Redox	Reduction-oxidation reaction

RF	Radio frequency
RHE	Reversible hydrogen electrode
SFG	Sum frequency generation
SHE	Standard hydrogen electrode
SPEC	Spectroelectrochemistry
TEM	Transmission electron microscopy
TOPAS	Travelling-wave optical parametric amplifier for super-fluorescence
UHV	Ultra-high vacuum
UV	Ultraviolet
VIS	Visible
w-MvK	Water-promoted Mars-van-Krevelen mechanism
WE	Working electrode
XANES	X-ray absorption near edge structure
XAS	X-ray absorption spectroscopy

List of Figures

1.1 Free energy diagram 2
1.2 Representation of possible reaction steps on a metal surface . 3
1.3 The electric double layer (EDL) model 4
1.4 Schematic representation of charge transfer and mass transport 6
1.5 Schematic representation of the d-band model 7
1.6 Sabatier's principle 8
1.7 Simplified Pourbaix diagram for gold in aqueous solution at 25 °C 9
1.8 Diagram on surface potential after initial gold oxidation 11

2.1 Representation of SFG generation 16
2.2 Principle of photoelectric effect 19
2.3 Gold subshell photoionization cross sections 21
2.4 X-ray absorption process 22
2.5 Representation of the laser system 24
2.6 Schematic of the Kerr mode-locking principle 24
2.7 Complete sum frequency set-up 26
2.8 Schematic representation of a synchrotron ring 27
2.9 Typical representation of a three-electrode cell 30
2.10 Principles of CV 31
2.11 Principles of CA 32
2.12 EC configuration for SFG measurements 33
2.13 EC for HP-XPS measurements 34
2.14 EC for HERFD-XANES measurements 34
2.15 Calibration of gold reference electrode 36
2.16 Schematic sketch of a mass spectrometer 37
2.17 Schematic of a quadrupole mass filter 38

3.1 SFG characterization of protocol 1 40
3.2 SFG characterization of protocol 2 42
3.3 HP-XPS spectra of gold oxide 43
3.4 HP-XPS spectra of OD-Au 44
3.5 Computed LSV and SFG for gold 46
3.6 Computed charge densities 47
3.7 Calculated nonlinear optical response change 47

3.8 Experimental HERFD-XANES spectra of gold oxide and metallic gold 50
3.9 *In situ* HP-XPS spectra of metallic gold and gold oxide 51
3.10 HP-XPS beam induced reduction study using two different X-ray beam fluxes 53
3.11 Catalytic tests on Au-TiO_2 and Au-γ-Fe_2O_3 55
3.12 Proposed w-MvK mechanism for CO oxidation 56
3.13 $C^{16}O$ oxidation over Au-γ-Fe_2O_3 with $H_2^{18}O$ and $^{16}O_2$ 57

1. Introduction

Chemistry defines every moment in our life: breathing, eating food, the use of cleaning products, the corrosion of metals, and so on. One of the branches of chemistry that makes modern life possible is catalytic chemistry. A catalyst reduces the activation energy for chemical reactions or open new reaction routes, as a result the overall process becomes faster and/or is performed at lower temperatures or pressure without the catalyst itself being consumed. We use catalytic processes to favour the formation of the products we need on daily basis. The term catalyst was coined by J. J. Berzelius in 1835[2] when he observed for the first time that some compounds, added in small amounts, could boost the decomposition of reagents in the system. This type of reaction has always been widely present in nature, *e.g.* in photosynthesis. Catalysts can be divided into three categories: homogeneous, which have the same aggregation state as the reagents; heterogeneous, which have a different aggregation state than the reagents; and biological, which are enzymes or enzyme complexes present in living systems.[3;4]

The chemical industry strongly depends on catalysts, and is always seeking new ones to improve the efficiency of chemical processes and increasing the selectivity for products. As a matter of fact, heterogeneous catalysis has played a central role in the chemical industry; some well-known examples are the Haber-Bosch process (1900s) which produces ammonia, and Fischer-Tropsch process (1920s) which produces hydrocarbons from syngas ($CO + H_2$).[5;6] It was estimated in 2005 that catalysts are used in the production of 90% of all commercially-produced chemical products.[7] Catalysts also provide a way to respond to new global challenges, *e.g.* shortage of resources accompanied driven by population growth, by building a more sustainable society through the use of green catalytic methods. Electrocatalysts, which are catalysts for electrochemical reactions, are an example of how catalysts are important for sustainable energy conversion and storage, and are key in the effective performance of electrolysers, fuel cells, and batteries, which drive our everyday life.

1.1 Surface chemistry

A chemical reaction can consist of one or several reaction steps. Improvements in catalysis can be achieved by understanding the steps involved in the formation and breaking of bonds at the surface of the catalyst where the interaction between reagents happens. Some examples of reaction steps are transition states, which describe a molecular configuration during the course of a reaction at a local maximum of energy, while intermediate states indicate a molecular configuration at a local minimum of energy, as shown in figure 1.1. From reactants to products, a catalyst decreases the activation energy of transition states which must be overcome for a chemical reaction to occur, opening the possibility of different reaction pathways. This is shown in figure 1.1. The lower the activation energy barrier, the faster the reaction rate.

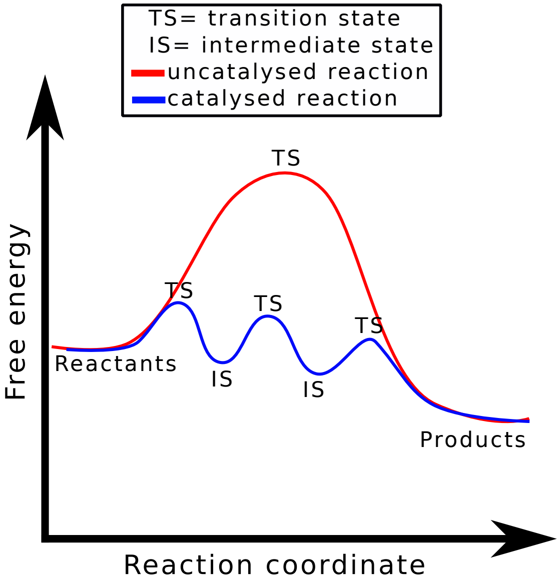

Figure 1.1: Free energy changes for a chemical reaction: the red curve is for an uncatalysed reaction, while the blue curve is for a catalysed reaction. TS means transition state, and IS is intermediate state.

The surface of a material is a region where there is a significant interaction with particles.[8] The activity and selectivity of a surface is defined by the interaction with the reagents,[9] such as: diffusion of the reactants to the surface; strength of the adsorption on the surface; presence of steps or vacancies; how easily the reagents react; and how easily the products desorb.

Adsorption means the adhesion to a surface (adsorbent) by liquid or gas molecules or dissolved molecules/ions (adsorbate). There are two categories of adsorption: physisorption, when van der Waals' forces are the main contributing interactions between adsorbent and adsorbate; and chemisorption, when there is a chemical bond between them.[10] The kinetics of chemical processes at the interface are main subjects of interest in *e.g.* catalysis, corrosion, etching, and chemical vapour deposition. In order to have a catalytic reaction, the adsorption of one or more reactants on the catalytic surface needs to be followed by the desorption of products. If the products do not leave the surface the catalyst is deactivated. Figure 1.2 shows some potential reactions steps on a metal surface, *e.g.* association/dissociation steps, diffusion, and inclusion.[11]

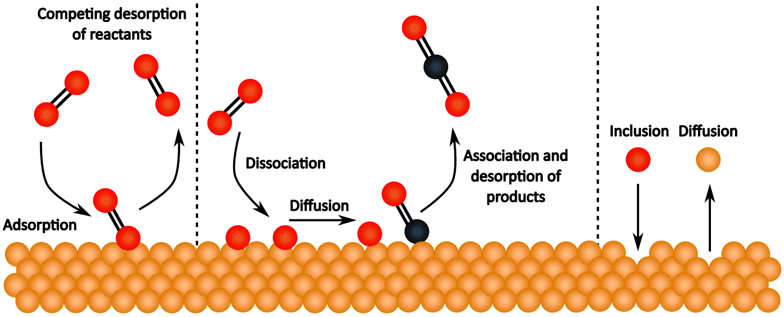
Competing desorption of reactants
Adsorption
Dissociation
Diffusion
Association and desorption of products
Inclusion
Diffusion

Figure 1.2: Representation of possible reaction steps on a metal surface: association/dissociation steps, diffusion, and inclusion. The catalytic activity is maintained if the products leave the surface of the catalyst.

1.1.1 Electrochemical processes at the interface

Electrochemistry focuses on the transport of charges between different chemical species. During these processes the oxidation states of the involved molecules change, called a reduction-oxidation (redox) reaction.[12;13] The name is due to the main processes involved: reduction, when a species gains electrons; oxidation, when another species loses one or more electrons. The reduction and oxidation processes happen simultaneously. Redox reactions take place through the natural release of chemical energy or by applying an external voltage. This process can be observed in an electrochemical cell (EC). There are two main types of ECs: electrolytic and galvanic.[14] An electrolytic EC creates a non-spontaneous reaction by putting energy into the cell, while a galvanic EC uses a spontaneous reaction to generate current.

The main parts of an EC are electrodes, an electrolyte, and the interface between them. An electrode is an electronic conductor of which there are two types: an anode, where the oxidation occurs, and a cathode, where reduction occurs.[14] Examples of electrodes are metals and carbon, like graphite and glassy carbon. An electrolyte is an ionic conductor containing a uniform amount of cations and anions (neutral solution), *e.g.* acidic and basic aqueous solutions, fused salts, and ionically conductive polymers.

Interactions between electrodes and ions from the electrolyte create an electric double layer (EDL), as shown by the first two planes of the simplified scheme in figure 1.3. In this model the solution is divided into several *layers*, and the whole structure has a thickness of 5-20 Å.[15] This idea is the result of different contributions by H. von Helmholtz, L. G. Gouy, D. L. Chapman, and

O. Stern.[14] Starting from a positively-charged electrode surface and moving out into the electrolyte there are:[16]

- *Inner Helmholtz Plane (IHP)*: which bisects the centre of specifically adsorbed species on the electrodes. Increasing the positive charge on the surface of the electrode, more anions will be attracted with respect to their concentration in the bulk.
- *Outer Helmholtz Plane (OHP)*: which bisects the counterions. These are solvated ions which only have long-range electrostatic interactions with the electrode, and they are defined as non-specifically adsorbed.
- *Diffuse layer*: here ions are distributed in a three-dimensional region because of thermal agitation in the solution. The excess charge decreases toward the bulk.

D. C. Grahame added that the molecules of the solvent can orient their dipoles on the interface, increasing the accumulated charge in the form of capacitive current at the IHP,[17] as represented in figure 1.3.

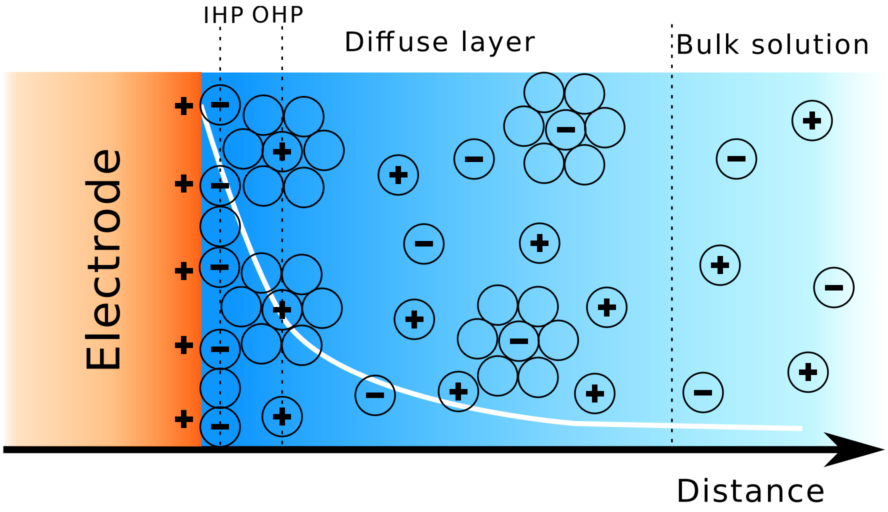

Figure 1.3: The electric double layer (EDL) model: inner Helmholtz plane (IHP) and outer Helmholtz plane (OHP). The white line describes how the electrochemical potential changes with increasing distance from the electrode.

Figure 1.3 also depicts how the electrochemical potential changes when moving far from the surface of the electrode as a white line. There is a linear behaviour between the IHP and OHP, then the potential decays exponentially in the diffuse layer.[18] The overall potential drop is usually of the order of 1 V.[15] Outside the diffuse layer, hence in the bulk, ions are not affected by the electrode potential. When there is no excess charge in both sides of the

EDL, the potential is called potential of zero charge; this value depends on the type of electrode, electrolyte solution, and its concentration.

Faradaic currents are generated when compounds are oxidised or reduced at electrodes. For this to happen, mass transport mechanisms towards the electrode are needed; these are diffusion in a concentration gradient, migration of ions in a potential gradient, and convection. When capacitive and Faradaic currents are flowing simultaneously, only their sum is measurable. The analytic signal is a sloping line for the capacitive current versus applied potential, which does not depend on the concentration of the analyte, while a Faradaic current makes a characteristic peak shape whose intensity depends on the analyte concentration.[18] Only when the molecules or ions are transported to the interface, and the product moves away from it, can a reaction at the electrode happen. The reaction rate at the electrode is defined by the mass transport of reagent/product to/from the electrode, and the charge transfer rate. The mass transport rate is affected by hydrodynamic conditions (e.g. rate of stirring the solution or rate of rotating the electrode, etc.), while the charge transfer rate depends on the chemistry of the system. If the the charge transfer rate is higher than the mass transport rate, the reaction is reversible and can be described by the Nernst equation.[18] In these conditions, Nernst equation provides the surface concentrations of the reduced and oxidized species at equilibrium with the electrode potential:

$$E = E^0 + \frac{RT}{nF} ln(\frac{C^O}{C^R}) \tag{1.1}$$

where E^0 is the standard potential, R is the gas constant, T is the temperature, n is the stoichiometric number of electrons in the reaction, F is the Faraday constant, C^O and C^R are the bulk concentration for the oxidised and reduced species, respectively.

Processes at the interface can happen at different timescales: ion diffusion/migration or macroscopic structural rearrangements (e.g bubble formation) are on the order of 100 ms; ion exchange/intercalation or molecular structural rearrangements take around 0.1–0.01 ms; bond breaking/formation, electron tunnelling and isomerization are in the ultrafast range,[19;20] meaning less than a nanosecond, as marked in figure 1.4. Electrochemical detection systems can probe mechanisms at nanosecond timescale or slower, meaning steady-state conditions are measured. In this thesis, steady states of the formed gold oxides are probed to investigate the structural changes of gold films after oxidation and reduction processes.

Although not investigated here, to probe mechanisms at nanosecond timescale or faster, a pump-probe detection system is needed. First, a pump pulse generates a nonequilibrium condition (e.g. the excitation of electronic or vibrational states), then a probe pulse interacts with the system in a different steady state while re-equilibrating after some time delay. The time

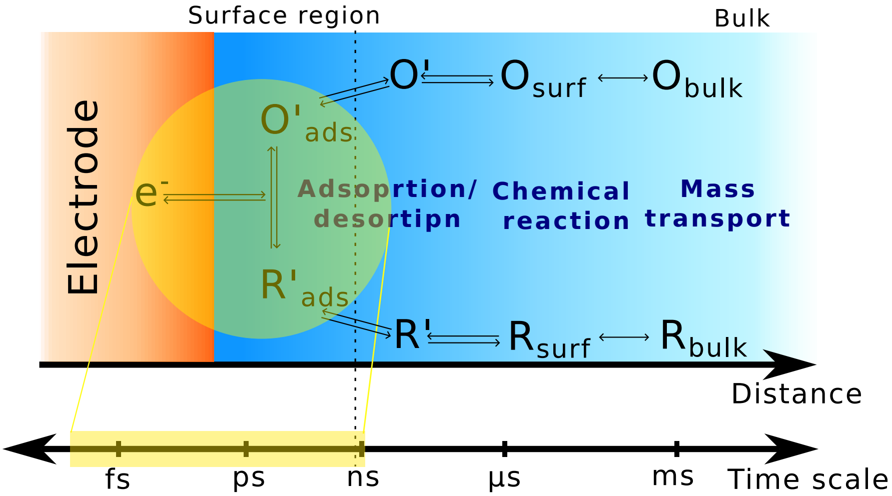

Figure 1.4: Schematic representation of charge transfer at the surface region and mass transport at the bulk region. When the charge transfer rate is higher than the mass transport rate, the electrochemical system is reversible. The yellow circle highlights the processes that happen at the ultrafast time scale at the surface region, such as electron tunnelling and isomerization.

resolution is defined by the pulse width of the lasers and the delay between pump and probe pulses.[19]

In summary, the processes at the metal surface are influenced by the electrolyte via the ion distribution in the electric double layer, the pH near the electrode, and amount of adsorbed ions.[21] The presence of the electrolyte near the metallic surface can modify its chemical structure under reaction conditions, hence *in situ* techniques are helpful to investigate the surface structure in the electrochemical environment.

1.2 Properties of gold

1.2.1 The d-band model

From ancient Egypt to now, gold has been considered a valuable material for ornament, jewellery, and currency.[22] It is one of the few metals found pure in its metallic state in nature, a so-called native metal. Chemically, it is a transition metal with a $5d^{10}6s^{1}$ electron shell, and belongs to the group 11 of the periodic table. The energy gap between 5*d* and 6*s* orbitals of gold is small, hence the absorbance is in the visible region starting around 521 nm. Like the other *d* elements, its chemistry is defined by the energy and reactivity of the *d* electrons.

For transition metals (3*d*, 4*d*, 5*d*), the d-band model of B. Hammer and

J. K. Nørskov is an important tool in heterogeneous catalysis development and is depicted in figure 1.5. It describes the interaction between adsorbates and a metal based on the position and filling of the *d* band of that metal.[23] The characteristics of the bonds between adsorbates and metals are defined by the d-band position with respect to the Fermi level and the *d*-band splitting into bonding and antibonding states. The occupation of these states defines the strength of the bonds. The strength of the bond is given by the *d* bands moving up in energy after interacting with an adsorbate, and as a consequence more antibonding adsorbate–metal *d* states become empty if they are above the Fermi level.[24] Otherwise, the metal is not able to bond and is defined as noble. This is usually the case for gold, but external conditions, like the application of a proper electrochemical potential, favours its oxidation.

When analysing chemical bonds, the Pauli principle needs to be considered, which states that *no two electrons in an atom can have the same set of four quantum numbers.* Attractive interactions and Pauli repulsion are both present during bond formation; when the former is bigger, bond formation is favoured. Pauli repulsion, however, is larger for the 5*d* metals (including gold) than the 4*d* and 3*d* metals. Gold has well-extended *d* states, which provoke a strong repulsion and result in noble behaviour.[23]

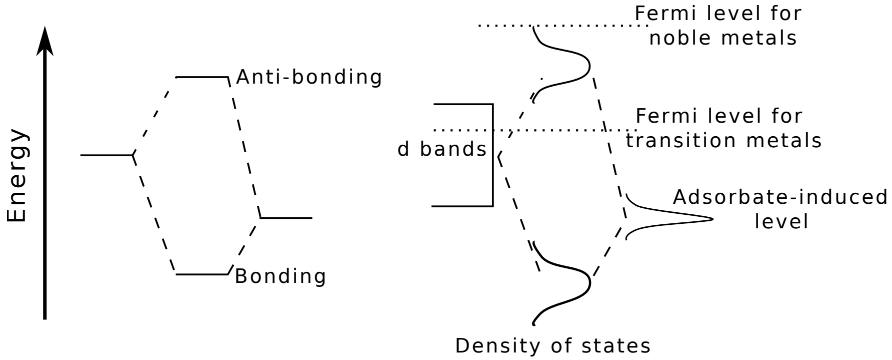

Figure 1.5: Schematic representation of the d-band model. *On the left:* Two sharp atomic or molecular states. *On the right:* An interaction between an adsorbate state and a metal surface. For noble metals, the anti-bonding state is completely filled below the Fermi level, which hinders bond formation between adsorbate and metal.

In catalysis, the efficiency of a catalyst for specific chemical reactions is depicted by Sabatier's principle,[25] which states that the best catalysts should interact with an intermediate strength with atoms and molecules, in such a way that reactants are activated and the products can desorb. This behaviour is illustrated by a volcano plot, shown in figure 1.6. As already mentioned, for transition metals the strength of a bond with an adsorbate is given by the energy of the anti-bonding states and their occupation. Towards the left in the d-block of the periodic table, a lower activation energy is needed for bond formation, but the reactants bond strongly and there is less free surface area available to catalyse the chemical process.[26] On the other hand, towards the right side of the d-block the lifetime of the reactants involved in the reaction on the surface is not long enough. Therefore, a compromise is needed when transition metals are used as a catalyst, called the Sabatier optimum.

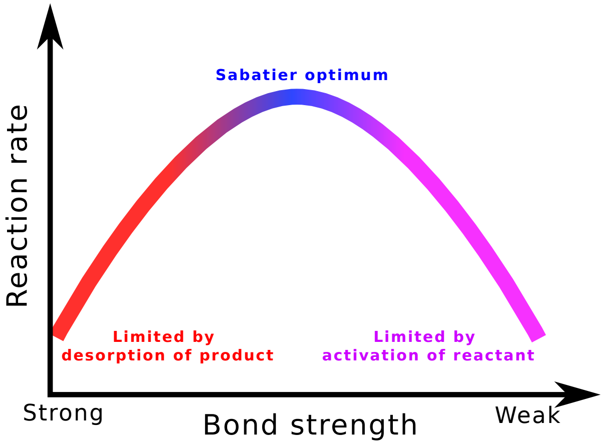

Figure 1.6: Volcano plot which gives a qualitative representation of Sabatier's principle.

1.2.2 Electrochemistry of gold

One of the initial uses of gold in electrochemistry was the electrolysis of water, the first experiment of which was done with two gold electrodes by A. Paets van Troostwijk and J. R Deiman 1789.[27;28] Water splitting is a key factor a sustainable solution to the current energy storage problem. The interesting reaction product is hydrogen, which can be stored and converted back into electricity by performing the opposite process in a fuel cell. Even though, the first experiment of electrolysis of water was over 200 years ago, consensus about the chemical processes involved has still not been reached.

Gold is an interesting metal since it is the only one which is thermodynamically stable within the stability potential window of water.[28;29] This behaviour is summarised in a Pourbaix diagram, a phase diagram which shows the equilibrium potentials (versus standard hydrogen electrode, SHE) of chemical reactions as a function of pH and show in which conditions chemical species are stable. This diagram is named after M. Pourbaix, who defined it in the early '50s.[30] Figure 1.7 depicts this system in a simplified way, lines *1* and *2* are boundary lines that represent the stability of solid species (AuO_2 and $Au(OH)_3$), where the orange area indicates soluble species

(*Au*$^{3+}$) and the cyan area is for the deprotonation of auric acid. Lines *3* and *4* are boundary lines for the stability of liquid water.[31] Potentials greater than the ones marked by line 3 oxidise water to oxygen, while potentials lower than those of line 4 reduce water to hydrogen. Oxidised species of gold can be produced at potentials above line 2, otherwise water reduces them to gold metal at all pH values. Since gold is not affected by strong acids and bases, this diagram quantitatively explains why it is defined as a *noble* metal.

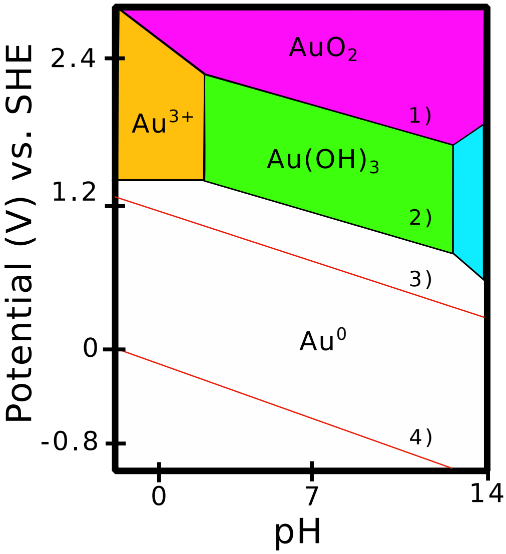

Figure 1.7: Simplified Pourbaix diagram for gold in aqueous solution at 25 °C, adapted from Pourbaix's *Atlas of electrochemical equilibria in aqueous solutions.*[30]

The gold in electrochemically-produced gold oxides mainly occurs as *Au*$^{3+}$, as proven by different independent experiments,[32–34] but there are many interpretations of the chemical composition of gold oxides from both experimental and theoretical studies, which might not be consistent with the Pourbaix diagram. Some of them postulate the following:

- Peuckert *et al.* claim that the first oxide layer covering the metal surface is $Au(OH)_3$, from 2 V vs. RHE this layer is deprotonated or dehydrated to *AuOOH* in 0.5 M H_2SO_4.[32]

- Xia and Birss concluded that below 1.5 V vs. RHE there is a thin layer of *AuO*, and above this potential there is a mixture of *AuO* and Au_2O_3. Au_2O_3 (α oxide) can form up to three monolayers, then a thicker oxide film is formed (β oxide) in 0.1 M H_2SO_4.[35]

- Koper *et al.* with density functional theory (DFT) calculations find:

$Au(OH)_3$ at 1.17 V vs. RHE, $AuOOH$ (α oxide) at 1.28 V which is dehydrated to Au_2O_3 (β oxide) at 1.54 V. From 1.95 V on OER starts.[36]

- Yang and Hetterschied show that the type of gold oxide is mainly due to the pH: $Au(OH)_3$ (β oxide) forms in alkaline media, and $AuOOH$ (α oxide) forms in acidic media.[37]

Usually α and β oxides are used to indicate two different types of oxide deposits: compact monolayers and hydrous layers on top, respectively.[38] In acidic conditions, from around 1.9 V vs. RHE β oxide promotes the oxygen evolution reaction (OER), while below -0.2 V vs. RHE gold metal catalyses the hydrogen evolution reaction (HER).[38;39] In basic conditions, the OER starts around 1.6 V vs. RHE, and HER around -0.5 V vs RHE.[38;40] The OER and HER are affected by pH conditions because they have Nernstian behaviour.

The initial stages of gold oxide growth have been investigated with many electrochemical quartz crystal micro- and nanobalance studies. With this methodology, oxide film formation and its reduction are mass-probed during electrochemical investigations. Xia and Birss[35] with Conway *et al.*[41] have proposed that the initial oxide formation is a two-electron process:

$$Au + H_2O \rightarrow Au/O_{ads} + 2H^+ + 2e^- \tag{1.2}$$

$$Au/O_{ads} \rightarrow O/Au \tag{1.3}$$

Mechanism 1.2 agrees with the change of mass observed experimentally. Mechanism 1.3 is a place-exchange process, which does not cause a detectable change in mass but modifies of the electronic interface with the solution. The place-exchange process moves the system away from equilibrium, facilitating the oxide growth.

Considering the time dependency of the gold oxide growth, Conway *et al.* proposed that, in acidic conditions, the early stages of gold oxide formation follows a logarithmic growth ($q \sim \log t$, with q as the amount of oxide and t as time) with two-dimensional structures of O below a monolayer, and an initial quasi-three-dimensional film formation post-monolayer.[42] The growth is trigged by place exchange between O and Au species, described as:

$$\frac{1}{F}\frac{dq}{dt} = k\,exp^{-(\Delta\phi - \Delta\chi_t)\frac{2\beta\mu N_A}{dRT}} \tag{1.4}$$

$$\Delta\chi_t = \chi_0 - 4\pi N_A \frac{q}{F}\mu \tag{1.5}$$

where $\Delta\phi$ is the electrostatic potential difference of the surface dipole array of O on the gold surface in a way that $\frac{dq}{dt}$ increases with $|\Delta\phi|$; $\Delta\chi_t$ is the charging surface potential with time; β is the barrier symmetry factor; μ is the dipole moment; N_A is Avogadro's number; d is the electrically effective thickness of the Au-O dipole; and R and T are the gas constant and the temperature, respectively. Figure 1.8 depicts a diagram of the surface potential after the initial gold oxidation and shows the roles of some of the parameters in equations 1.4 and 1.5.

Tremiliosi *et al.*[43] suggested that in acidic condition there is a logarithmic growth up to two monolayers due to the interfacial place exchange between gold atoms on the surface and chemisorbed oxygen atoms; after three monolayers the growth is inverse-logarithmic and limited by the breakout of a gold cation at the metal side of the metal/oxide interface into the oxide.[43]

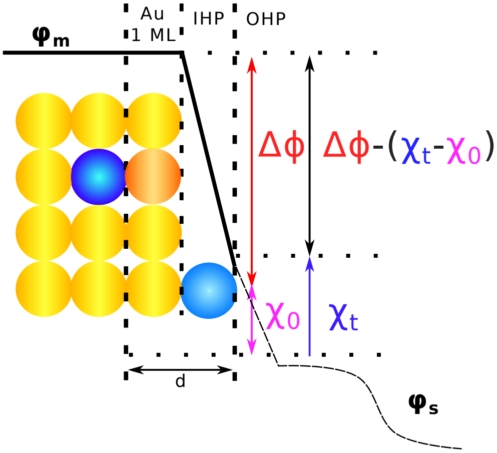

Figure 1.8: Schematic diagram of the model from Conway *et al.*[42] showing how the surface potential of gold changes during the initial oxidation stages. Metallic gold is shown in yellow, gold after place exchange in orange, adsorbed oxygen in light blue, and oxygen below the gold surface after place exchange in dark blue. *IHP* stands for inner Helmholtz plane and *OHP* for outer Helmholtz plane. φ_m and φ_s are the inner metal and inner electrolyte potentials, respectively. $\Delta\phi$ is the surface potential, χ_0 is the initial surface potential due to $Au^{\delta+}$–$O^{\delta-}$ dipoles, and χ_t is the time-dependence surface potential after place exchange ($O^{\delta-}$–$Au^{\delta+}$ dipoles).

1.2.3 Gold as a catalyst

Gold was long-considered generally chemically inert. However, it has been shown recently that, when its dimensions are in the nanometre scale and/or in support metal oxides, gold presents catalytic properties.[44–49] The pioneering work of Haruta *et al.* in 1989 was one of the first studies on gold as catalyst.[50] It focused on low-temperature CO oxidation by gold nanoparticles supported in transition metal oxides, which is an important reaction for both environmental and catalytic studies.[51] Currently, the reaction steps are still unclear, but gold oxide was suggested to be actively involved in the CO oxidation process.[52–54] It is important to note that gold is not only able to catalyse CO oxidation to CO_2, but also to reduce it back to CO with proper working conditions. The revaluation of gold's properties has driven an interest in acquiring a fundamental understanding of the chemical processes on gold surfaces, with the aim of designing gold-based catalysts. In this thesis three forms of gold materials are examined: gold oxide (as discussed in the previous section) from gold films, oxide-derived gold (OD-Au) from gold films, and gold nanoparticles (Au NPs) supported on metal oxides (TiO_2 and Fe_2O_3).

Oxide-derived (OD) metals are generated by reducing an oxide precursor, e.g. in aqueous phase or in gas phase. OD coinage metals show improved catalytic activities towards CO_2 reduction relative to their pure polycrystalline metal counterparts.[55–58] Gold, as an electrode material, has one of the highest activities and selectivities for CO_2 reduction to CO among the polycrystalline metals,[59;60] which is enhanced in OD-Au.[61;62] One possible explanation is better stabilization on the surface of OD-Au of the one-electron-reduced $CO_2^{\bullet-}$ intermediate.[61] Another study suggested that metastable, highly-active surface structures on OD-Au caused by defects, e.g. grain boundaries or linear dislocations generated and kinetically trapped during the oxide reduction, could be involved in its improved catalytic performance.[63] Surface OD nanoporous gold produced from electrochemical dealloying of $Ag_{70}Au_{30}$ has shown a Faradaic efficiency of 90% for a CO_2-to-CO reduction process.[62] The enriched catalytic activity of surface OD nanoporous gold over clean nanoporous gold might be due to a low concentration of chemically inert surface/subsurface gold oxide species created from the electrochemical dealloying. However, most of the oxygen from the oxide could be removed during electrochemical analysis or CO exposure, while the remnants seem to be quite stable and capable of modifying reactivity and selectivity. Defects resulting from the gold oxide reduction were also suggested as an explanation of the improved performances. There is still an open debate about the reasons behind the better catalytic activity of OD-Au, including the possible role of subsurface oxide remnants.[57]

Supported Au NPs catalysts have their catalytic properties defined by the chemical composition of the support, the size of the gold particles, and the structure of Au-support interface. The support is usually a metal oxide. Metal oxides supports are classified as reducible or non-reducible relative to their capability to remove oxygen from the structure to form oxygen-deficient structures or non-stoichiometric compounds.[64] Titanium dioxide (TiO_2), nickel(II) oxide (NiO), and iron(III) oxide (Fe_2O_3) are examples of reducible oxides. Zinc oxide (ZnO), magnesium oxide (MgO), and zirconium dioxide (ZrO_2) are non-reducible oxides. The size of the gold particles is important for the CO oxidation performance, and it has been suggested that a size of 2–3 nm is optimal for CO oxidation in Au/TiO_2.[65] Some suggested mechanisms for the CO oxidation are: Langmuir-Hinshelwood (LH), in which the products are the result of the interaction of coadsorbed reactants on the surface of the catalyst; and Mars-van Krevelen (MvK), in which the products have one or more constituents from the support. Further complicating the analysis of the CO oxidation reaction is the debated role of adventitious water; it has been suggested to be either inactive or active via proton transfer.[66]

1.3 This thesis

This thesis presents electrochemical and catalytic studies of different gold surfaces, whose scientific manuscripts are attached at the end. An introduction about the characterization techniques precedes the discussion of the results.

In **Paper I**, electrochemically-formed OD-Au in acidic conditions (1M H_3PO_4, pH 1) are investigated with *operando* sum frequency generation (SFG) and *ex situ* high pressure X-ray photoelectron spectroscopy (HP-XPS) to prove the presence of gold oxide remnants (as Au_2O_3 or $Au(OH)_3$) beneath the topmost gold layer when the OD-Au is formed. To better interpret the SFG data, further investigation of the gold oxide in acidic conditions was conducted to examine changes in the electronic structure through mathematical models coupled with experimental measurements in **Paper II**. In addition, to better understand the chemical composition of the gold oxides formed during oxidation and the beam induced effects on the sample, *in situ* HP-XPS and *operando* high energy resolution fluorescence detected X-ray absorption near edge structure (HERFD-XANES) methods are compared and presented in **Paper III**.

In **Paper IV** experimental catalytic tests are done on low-temperature CO oxidation on Au-γ-Fe_2O_3 and Au-TiO_2. Mass spectrometry is employed and different oxygen isotopes (^{16}O and ^{18}O) are used to discriminate the reaction steps of CO and H_2O. This study suggests that water-promoted CO oxidation on Au-γ-Fe_2O_3 is through Mars-van-Krevelen (w-MvK) reaction, which means the products have one or more constituents from the support and water. On the other hand, CO oxidation on Au-TiO_2 follows a Langmuir-Hinshelwood (LH) mechanistic process, which means the reaction happens only between adjacent adsorbed reaction intermediates on the surface of the catalyst.

2. Methods

This chapter outlines the characterisation techniques used to generate the data presented in chapter 3 of this thesis. A theoretical background, including practical details, is followed by a description of the equipment. Measurements were conducted at the *Physics Dept.* and the *Material and Environmental Chemistry Dept.* at Stockholm University and at *Deutsches Elektronen-Synchrotron (DESY)* in Hamburg, Germany.

2.1 Spectroscopic techniques

Spectroscopy, from Latin *speciō* and Greek *σκοπειν* – both from verbs meaning *to see* – is the study of interactions between light and matter. Discrete energy levels are investigated via absorption or emission of the incident electromagnetic radiation. The detected signal describes the generated transitions, as a function of intensity and energy, which provides information on the properties of the sample. The electromagnetic spectrum can be divided into different energetic regions which provide distinct information: terahertz (THz, $\sim 0.001 - 0.01$ eV) for e.g. low frequency dielectric relaxation and conductivity, infrared light (IR, $\sim 0.01 - 1$ eV) for rotational and vibrational excitations which are linked to molecular structure and bond strengths; ultraviolet to visible light (UV-Vis, $\sim 1 - 300$ eV) for transitions between molecular orbitals which are linked to valence orbitals and their electrons; X-ray light (~ 300 eV – keV) to probe localized core electrons and core to valence transitions; gamma-ray light (MeV) for very strong ionizations. Of particular interest in this thesis is X-ray light, which can be divided in soft (≤ 1 keV), hard (≥ 5 keV), and tender (in between) energies. The rest of this section introduces the spectroscopic techniques employed in the work presented in this thesis: optical SFG, which uses IR and VIS light; and XPS and XAS, which here are both in the hard X-ray regime.

2.1.1 Optical sum frequency generation spectroscopy

Sum frequency generation (SFG) spectroscopy is a type of nonlinear technique, which is non-invasive and interface-sensitive, and is used to investigate molecular chemistry and dynamics.[67] It consists of the overlap in space and time of two photons with different frequencies, and as a result a photon with a frequency equal to the sum of the initial photons is released.[68]

Second harmonic generation (SHG) is a specific form of SFG in which both input photons have the same frequency. SFG occurs after the interaction with a medium having a non-vanishing second order nonlinear susceptibility. Though the theory was already developed in the early '60s, the first experimental work was done by Y. R. Shen *et al.* only in 1987 thanks to progress in laser technology.[69;70] Since then, more experimental and theoretical work has been done to understand the SFG spectra and improve the design of SFG experiments, which has become a fundamental tool in surface science.[71–73]

The work presented in this thesis was obtained using visible (VIS) and infrared (IR) incident photons, hence only this case is considered from now on. A schematic representation of SFG is depicted in figure 2.1. The input electric fields (E_{IR} and E_{VIS}) interact with the molecules at the surface inducing a second order nonlinear polarization ($P^{(2)}$) defined as:

$$P^{(2)}(\omega_{VIS}+\omega_{IR}) = \chi^{(2)} E_{VIS}(\omega_{VIS}) E_{IR}(\omega_{IR}) \tag{2.1}$$

where $\chi^{(2)}$ is the second-order nonlinear susceptibility.

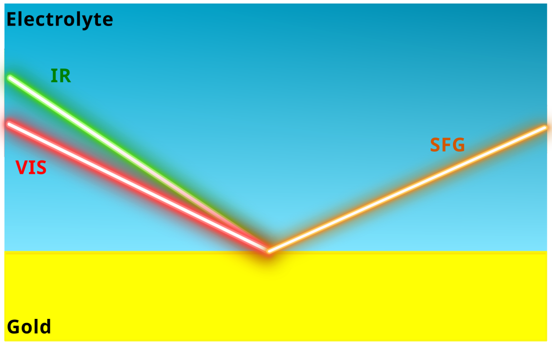

Figure 2.1: Description of SFG generation. Energy and parallel momentum are conserved: $\omega_{IR} + \omega_{VIS} = \omega_{SFG}$; $k_{//}^{IR} + k_{//}^{VIS} = k_{//}^{SFG}$.

To understand the surface sensitivity of SFG, consider inverting the sign of the incoming electric fields.[74] As a consequence, the induced polarization must also change sign. When a medium has inversion symmetry, $\chi^{(2)}$ does not invert its sign, and equation 2.1 becomes:

$$-P^{(2)}(\omega_{VIS}+\omega_{IR}) = \chi^{(2)}(-E_{VIS}(\omega_{VIS}))(-E_{IR}(\omega_{IR})) \tag{2.2}$$

In order for equations 2.1 and 2.2 to be satisfied at the same time, $P^{(2)}(\omega_{VIS}+\omega_{IR})$, and therefore $\chi^{(2)}$, must be equal to zero. This implies that when a medium has inversion symmetry SFG is forbidden, but is allowed at the interface since the symmetry is broken. However, the bulk contribution cannot be removed completely.[70]

The second-order nonlinear susceptibility can be written as:

$$\chi^{(2)} = \chi^{(2)}_{RES} + \chi^{(2)}_{NR} \tag{2.3}$$

The first parameter $\chi^{(2)}_{RES}$ describes the vibrationally resonant term from the adsorbate. When the IR field is in resonance with the frequency of a molecular vibrational mode, $\chi^{(2)}_{RES}$ is greatly enhanced. This contribution is nonzero only when both IR and Raman transitions are spectroscopically allowed.[74] In other words, when a vibrational mode is both IR and Raman active, it is also SFG active.

The second parameter $\chi^{(2)}_{NR}$ is the non-resonant contribution originating mainly from the substrate, which is typically quite large when dealing with metal surfaces. $\chi^{(2)}_{NR}$ can be defined as:[75]

$$\chi^{(2)}_{NR} = B_{NR} \cdot e^{i\Phi} \tag{2.4}$$

The SFG intensity is proportional to the square modulus of the sum of resonant and non-resonant signals:[75;76]

$$I_{SFG} \propto |B_{NR}|^2 + |\chi^{(2)}_{RES}|^2 + |B_{NR}||\chi^{(2)}_{RES}| cos[\Phi - \delta(\omega)] \tag{2.5}$$

where $\delta(\omega)$ is the frequency-dependent phase of the resonant spectrum. The cross-term amplifies the non-resonant signal, leading to a broad signal from metal surfaces. In **Papers I and II** in this thesis, the SFG data was collected using wavelengths that only provide a non-resonant SFG response from gold surfaces.

To model this SFG response, Mendoza *et al.*[77] followed by Busson and Dalstein[78–80] considered the electron density as the sum of the contributions of free electron gas (n_e^f) and bound electrons (n_e^b):

$$n_e = n_e^f + n_e^b \tag{2.6}$$

To model a system composed of a thin surface layer on top of a bulk metal, the effective $\chi^{(2)}_{NR}$ is described as:

$$\chi^{eff} = \chi^{eff,S} + \chi^{eff,B} = \chi^{eff,f} + \chi^{eff,b} \tag{2.7}$$

where S and B mean surface and bulk, respectively; and each $\chi^{eff,S/B,f/b}$ for a PPP polarization combination is:

$$\chi^{eff,S/B,f/b}_{ppp} = F_{zzz}\chi^{S,f/b}_{zzz} - F_{xxz}\chi^{S,f/b}_{xxz} - F_{xzx}\chi^{S,f/b}_{xzx} + F_{bulk}\chi^{B,f/b} \tag{2.8}$$

Here, the Fresnel factors (F) are computed using the bulk metal dielectric function. More details are presented in **Paper II** and in Busson and Dalstein's work.[79] Adsorption of compounds modifies the electron density on the surface. When an oxygen atom chemisorbs on gold, its large electronegativity moves the electron density towards itself, causing a redistribution of the metal electrons and a reorientation of water dipoles. Based on Walters and Roy's work,[81], the change in the free electron density is:

$$\Delta n_e^{S,f} = -\frac{\sigma_m}{e l_n} \tag{2.9}$$

where σ_m is the charge density on the metal surface, l_n is the distance in which there is a change of the surface charge density, and e is the electric charge. The variation of $\chi^{eff,S,f}$ is due to equation 2.9 if the free electron polarizability is constant. However, there is also a chemisorption bond formation between O $2p$ and Au $5d$ electrons, which affect the bound electron density at the surface. Like the free electron density, the bound electron density is described by:

$$\Delta n_e^{S,b} = -\frac{\sigma_{ad}}{e l_n} \tag{2.10}$$

where σ_{ad} is the adsorbed charge density. Hence, $n_e^{S,b}$ is modified by the adsorption, which changes the $\chi^{eff,S,b}$, when the electron polarizability of the bound electrons is approximated to be the same as the bulk one as in **Paper II**.

SFG measurements can be done under different polarization combinations: SSS (S-polarized SFG, S-polarized VIS, and S-polarized IR), SSP, SPS, SPP, PSS, PSP, PPS, and PPP.[82;83] Metallic surfaces usually have high reflectivity values in the IR region, and as a consequence the surface electric field is large in the z direction and small in the x and y directions. Gold substrates reflect more than 97% of the incident IR beam, hence only resonant susceptibilities with a z infrared component give a significant SF signal.[76] The non-vanishing resonant susceptibilities are $\chi^{(2)}_{zzz}$, $\chi^{(2)}_{xxz}$ and $\chi^{(2)}_{xzx}$ for PPP, and $\chi^{(2)}_{yyz}$ for SSP. In **Paper I and II** the PPP polarization was used to collect experimental data since it yields the highest SFG intensity. The presence of water in the electrochemical cell on top of the gold surface attenuates the resulting SFG signal, reducing its intensity, but the PPP polarization still resulted in good-quality data.

2.1.2 X-ray photoelectron spectroscopy

X-ray photoelectron spectroscopy (XPS), also known as electron spectroscopy for chemical analysis (ESCA), is a surface-sensitive technique that allows the detection of chemical states, hence the chemical composition of the material under investigation is examined. XPS was developed by K. Siegbahn[84] in the '50s, building upon A. Einstein's explanation of the photoelectric effect from 1905.[85] The discovery of this effect is dated back to 1887 by H. Hertz. When a photon (here an X-ray photon) interacts with an atom, the energy might be transferred to an electron. As a consequence, if there is sufficient energy, that electron will be ejected with a kinetic energy (KE) equal to the difference between the initial photon energy ($h\nu$) and the binding energy (BE) of that electron according to conservation of energy. The left side of figure 2.2 shows this process. XPS is a surface-sensitive technique because electrons from the bulk have to travel a longer distance than the electrons from the surface. The probability of inelastic collisions therefore becomes significantly higher, which prevents those bulk electrons from reaching the continuum.

The BE is specific to the core-hole state of the atomic/molecular orbital level from which the electron is released:

$$BE = h\nu - KE - \phi s \tag{2.11}$$

where ϕs is the work function of the spectrometer. The information of the chemical composition originates from the BE of the emitted electrons of the sample under investigation. Different chemical environments influence the BE of the atom/molecule under investigation. As a result, the BE can be defined as follows:

$$BE = E_i - E_f \tag{2.12}$$

where E_i is the initial state of the electronic ground state, and E_f is the final state which is a core-hole state caused by the effects of absorption of the incident photon and/or ejection of the electron from system.

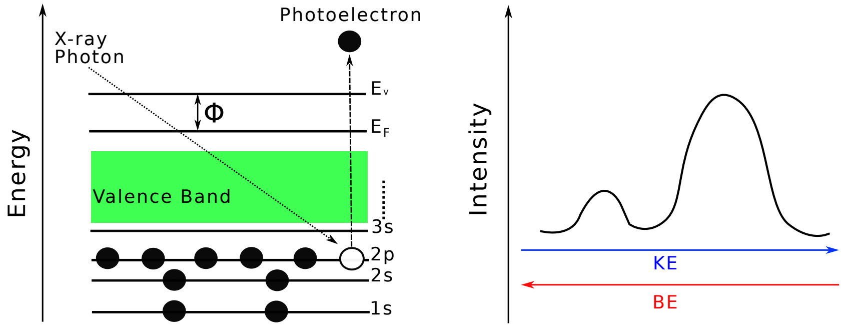

Figure 2.2: *Left:* Schematic representation of photoelectric effect after exposure to a X-ray photon. *Right:* Example of an XPS spectrum showing the relationship between kinetic energy (KE) and binding energy (BE).

The detection system (electron analyser) measures the KE of the ejected electrons and from equation 2.11 the BE is calculated. The outcome is counts (number of electrons per unit of time) as a function of the BE represented by a spectrum with one or several peaks, as shown on the right side of figure 2.2. Each peak describes a characteristic surface species or adsorbate, and its area is proportional to the number of atoms for that species. The width of the peak is mainly due to the life time of the core-hole state, the beam energy width, and the resolution of the spectrometer. Sometimes, chemical shifts can be small and not well-separated. In these cases, a peak fitting is needed to identify all the different contributions from the surface species. First, a background caused by inelastically scattered electrons is subtracted by using a Shirley, Tougaard, or linear algorithm.[86;87] Then a Lorentzian function, a Gaussian function, or a convolution of them (Voigt function) is usually employed to fit the peaks.[88]

Spin–orbit coupling is a quantum effect originating from the interaction of the magnetic fields from the orbital angular momentum (L) and the spin (S) when $L \neq 0$. An example is the $4f$ core level (azimuthal quantum number $l = 3$), which presents two peaks in an XPS spectrum, $4f_{7/2}$ and $4f_{5/2}$, whose BEs are the final states with total angular momentum $j_{+} = l + 1/2 = 7/2$ and $j_{-} = l - 1/2 = 5/2$, respectively.[89] The intensities of these two peaks are given by the degeneracy of each spin state, which is the number of spin combinations, resulting in total of $2j + 1$. The 4f-orbital core levels have an area ratio of 4:3, which needs to be considered in the peak fitting method. For the investigation of gold surfaces presented in this thesis, the BEs of gold $4f_{7/2}$ and $4f_{5/2}$ are at 84.0 and 87.6 eV, respectively. Depending on the degree of oxidation, the intensity of the two peaks decreases and a shoulder appears on the higher energy side of both peaks for most metals, which can even become the main peak in strong oxidising conditions. This shift towards higher BEs is explained by the higher electronegativity of binding oxygen atoms in the metal oxide.[90] Hence, in the oxygen $1s$ spectrum there is a shift towards lower BEs after oxidation for most metal oxides, including gold.

One drawback of conventional XPS is that a ultra-high vacuum (UHV) is typically needed during measurements, which limits what types of systems can be studied. This restriction has recently been overcome with the progress of synchrotron radiation sources. With modern synchrotron sources,[91] X-ray measurements can be performed at the triple-phase boundary between the gas phase, electrolyte, and electrocatalyst at higher (up to ambient) pressures,[92] called ambient-pressure or high-pressure XPS. **Papers I and III** use this technique.

The usage of hard X-rays enables the generation of photoelectrons with elevated KEs, in this way the inelastic scattering is reduced and the signal-to-noise ratio is improved from a triple-phase boundary system. Increasing the incident photon energy decreases the photoionization cross sections (PICS), as depicted in figure 2.3 for the case of gold.[93;94] The PICS is the probability that an incoming photon generates an electron photoemission process, and the intensity of the resultant spectrum is proportional to this. The PICS is highest near the ionization threshold, then it decays with increasing photon energy.

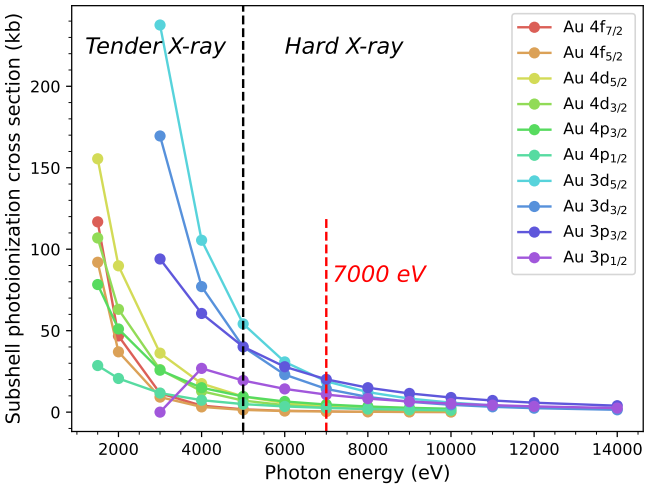

Figure 2.3: Gold subshell photoionization cross sections in kb (= 10^{-21} cm^2) as function of incident photon energy (eV). The data shown here is taken from Trzhaskovskaya and Yarzhemsky's work.[93;94] 7000 eV is the photon energy used for high pressure XPS measurements in **Papers I and III.**

2.1.3 X-ray absorption spectroscopy

Unlike XPS, which is executed with a fixed incident photon energy, X-ray absorption spectroscopy (XAS) measures the X-ray absorption intensity of matter as a function of a range of incident photon energies. The first XAS spectrum was recorded by H. Fricke in 1920.[95] In an XAS spectrum, a sharp peak in intensity indicates an absorption edge, which is the required energy to create a hole in the core level. Each core level has a spectroscopic name related to its principal quantum number: *K, L, M, ...* for n = *1, 2, 3, ...*, respectively. In addition, subscripts are added to indicate the splitting between atomic orbitals (*s, p, d, ...*), or a spin-orbit interaction between the projected angular momentum (m_l) and electron spin (m_s); such as K (1s), L$_1$ (2s), L$_2$ (2$p_{1/2}$), and so on. The probability of transition from an initial state $|i\rangle$ to a final state $|f\rangle$ is given by Fermi's *golden rule*:[96]

$$P_{if} = C|\langle f|\exp^{ikx} \cdot \boldsymbol{e} \cdot \boldsymbol{p}|i\rangle|^2 \rho_f(E) \tag{2.13}$$

where C is a constant that contains mass, speed of light and frequency; k is the wave vector ($2\pi/\lambda$); **e** is the spacial unit vector; **p** is sum of the linear momentum operators of the electrons; and $\rho_f(E)$ is the energy density of the final state. If the incident electromagnetic wavelength is larger than the distances between atoms/molecules, then the electromagnetic field can be approximated as constant over the atom/molecule ($k \cdot x \ll 1$); this is called the dipole approximation. Electronic transitions must follow the dipole selection rule, which states that only $\Delta l = \pm 1$ transitions are allowed.[96] The X-ray absorption cross section is:

$$\sigma = \frac{P_{if}}{F_{ph}} \tag{2.14}$$

where F_{ph} is the number of incident protons per unit time and area.

For the work presented in this thesis, attention is given to the energy region near an absorption edge containing unoccupied electronic levels below or at the vacuum level, as depicted in figure 2.4. The information in this energy range is element-specific and provides information on the chemical environment. This method is known as near-edge X-ray absorption fine structure (NEXAFS) or X-ray absorption near-edge structure (XANES) spectroscopy. XANES spectra have a characteristic main peak at the absorption edge, which is also called the *white line*. For example, this thesis considers the white line for gold at the L_3 edge, which is due to the $2p_{3/2}$ to $5d_{5/2,3/2}$ transition, and its intensity increases after oxidising since the oxidation causes new unoccupied states that can be filled by an electronic transition during an X-ray absorption process.

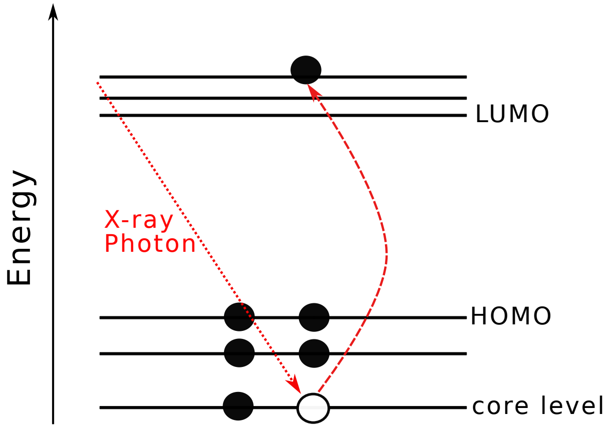

Figure 2.4: Schematic representation of X-ray absorption process for the case of XANES. The gap between highest-occupied molecular-orbital (HOMO) and lowest-unoccupied molecular-orbital (LUMO) is present for illustration purposes, it is not expected in gold.

XAS detection can be done through *e.g.* measurements in transmission, which provides direct access to the absorption cross section, or in fluorescence decay, which provides the fluorescence yield (probability to emit fluorescent photons per time and area) which is proportional to the number of core holes. XAS spectra generally have a low resolution for high-Z elements in the XANES region. To detect variations in the d-band occupancy of gold, for example during an oxidation process, with a higher resolution, the high-energy-resolution fluorescence detection (HERFD) method, developed in the mid ’80s by P. Eisenberger *et al.*,[97] can be employed. With HERFD, the emitted X-ray fluorescence line with an energy bandwidth similar to or below the core-hole lifetime of a distinct excited-state decay is measured. The fluorescence yield corresponds to the absorption cross section. In this thesis, the Au $L_{\alpha 1}$ emission was measured using HERFD-XANES, thus the improved spectral resolution is given by the $3d$ core hole which provides sharper peaks.

Electronic structure calculations are often used to simulate XAS spectra as the analysis of experimental spectra alone is not always straightforward. In **Paper III**, the FEFF code was employed, which uses the multiple-scattering real-space Green’s function formalism[98] whose many-body effect calculations have shown good agreement with experimental data.[99]

2.2 Light sources and detection systems

2.2.1 Optical set-up

Instrumentation for sum frequency generation (SFG) spectroscopy can be built for two different configurations.[100] One is called scanning, where both infrared (IR) and visible (VIS) laser pulses have a narrow bandwidth, and spectra are acquired by scanning over a broad IR region. The other is called broad bandwidth, where IR laser pulses have a broad bandwidth while VIS laser pulses have a narrow bandwidth. Only two frequencies, one per each region, are used. In this thesis, a broad bandwidth SFG system is employed and the following paragraphs explain in detail the optical set-up used for the measurements.

The solid-state laser system is composed of two main parts – a Ti:sapphire (Ti:Sa) oscillator and an amplifier – as shown in figure 2.5. The first part is pumped by an Nd:YVO_4 laser having a continuous wave (CW) output of 532 nm. The oscillator is subject to the Kerr self-focusing effect, a third-order nonlinear process in which the refractive index of the material, in this case Ti:Sa, is described as function of the intensity:

$$n(I) = n_0 + n_2 I \tag{2.15}$$

where n_0 is the linear refractive index, n_2 is the nonlinear refractive index, and I is the light intensity of the incoming beam. Here a Gaussian beam is present, hence the intensity varies according to this distribution. As a consequence, Ti:Sa acts as a lens, and this effect is called self-focusing. Since n_2 is quite small for Ti:Sa, this phenomenon happens with high peak power beams.[101;102] The optimization of this passive amplitude-modulation mechanism gives a high intracavity power, and generates femtosecond pulses (figure 2.6). The main drawback is the dispersion of group velocity caused by the crystal.[103] Brewster prisms are used to create a negative group velocity dispersion, which means the velocity of shorter wavelengths is increased.[104]

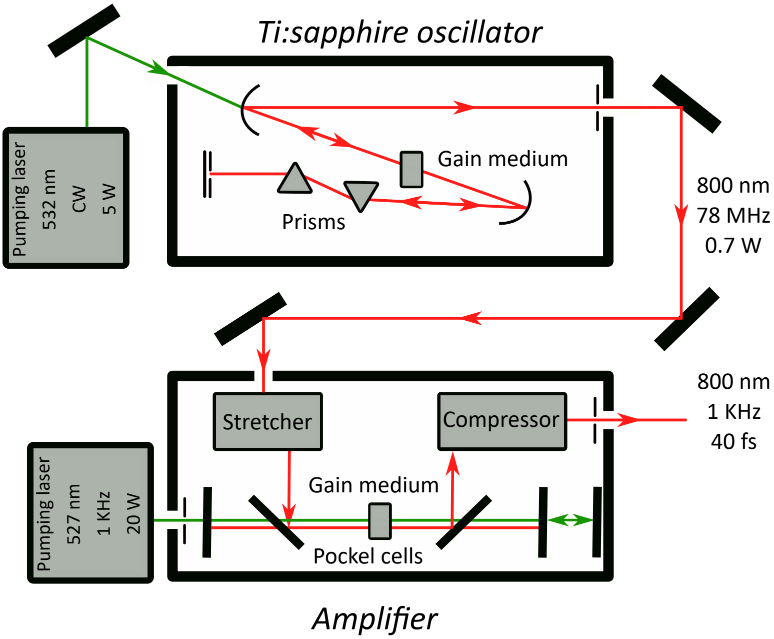
Ti:sapphire oscillator
Pumping laser
532 nm
CW
5 W
Gain medium
Prisms
800 nm
78 MHz
0.7 W
Stretcher
Compressor
800 nm
1 KHz
40 fs
Pumping laser
527 nm
1 KHz
20 W
Gain medium
Pockel cells
Amplifier

Figure 2.5: Representation of the laser system. Instrumentation from Coherent Inc.

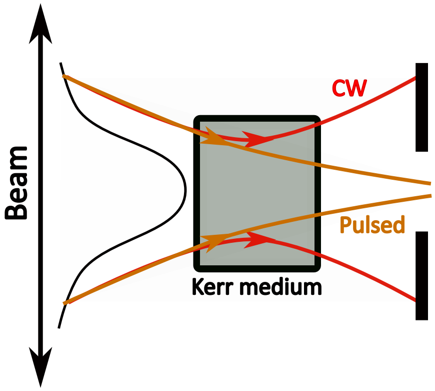
Beam
CW
Pulsed
Kerr medium

Figure 2.6: Schematic of the Kerr mode-locking principle. The Ti:sapphire crystal is the Kerr medium, which focuses the higher intensity region of the beam. High intensity modes are selected by an adjustable aperture.

The second part of the laser system, the amplifier, is composed of three sections – a stretcher, a regenerative amplifier, and a compressor – as shown in the bottom part of figure 2.5. The stretcher converts the laser pulses from femtoseconds to picoseconds. These new pulses reach the regenerative amplifier, which is pumped by a Nd:YLF laser (527 nm). Here, the light enters a cavity. In total there are two Pockels cells: the first one lets pulses in with a repetition rate of 1 KHz, then a Faraday rotator sends the pulses out when the polarization state has been switched (from vertical to horizontal); when a high amplification is reached, the second cell then releases the pulses into the compressor.[105] There, the pulses are compressed again, and the final output is a pulse beam of 40 fs full width at half maximum (FWHM) with a central wavelength of 800 nm and a repetition frequency of 1 KHz.

The rest of the optical set-up to generate the SFG signal consists of a travelling-wave optical parametric amplifier of super-fluorescence (TOPAS), a non-collinear difference-frequency generator (nDFG), a pulse shaper, and a delay stage. This complete set-up is shown in figure 2.7. In the TOPAS, a nonlinear crystal made of beta-barium borate (BBO) downconverts some of the 800 nm photons into two with total energy equal to that of the incoming photon. These two new pulses are called *signal* and *idler*, and they are in the near-IR region. The output generated by the TOPAS is split into two beams: the *signal* and *idler* photons are sent directly to the nDFG, while the unconverted one is directed to a pulse shaper.

The optical properties of BBO do not allow for direct conversion into mid-infrared.[74] Hence, another nonlinear crystal, $AgGaS_2$, is used to perform difference frequency generation between *signal* and *idler* in nDFG.[106] The output frequency is in the mid-IR range of the spectrum (2.6-11 µm) and is due to the difference of the two incoming beams, which are controlled from the TOPAS via software. The IR pulses used in this thesis are centred at around 3.5 µm, and as a result the SFG signal is maximised at 0.650 µm.

The 800 nm femtosecond pulses of the second beam from the TOPAS require a pulse shaper to control the spectral resolution of the experiment. This is done with a grating-lens system, which allows selection of a frequency range with a slit aperture. The pulses are narrowed to around 12 cm^{-1} and consequently the pulse length is increased to picoseconds.[11] A delay stage ensures the temporal overlap between the two beams at the EC. A 750 nm short-pass edge filter lets only the SFG signal from the EC enter the spectrometer (Andor SR-303I-A) and be detected by a charge coupled device (CCD) camera.[107]

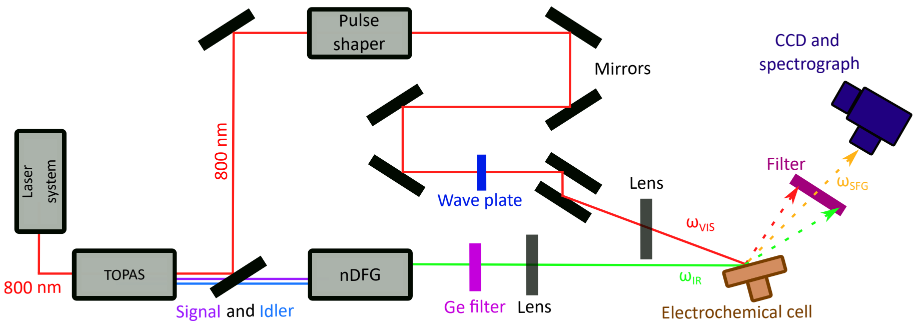

Figure 2.7: Complete sum frequency set-up. Instrumentation from Coherent, Inc.

2.2.2 X-ray generation: synchrotron radiation

Although lab-based sources of X-rays were more commonly used in the past, nowadays synchrotron radiation X-ray sources are preferred as they have higher brilliance (number of photons emitted per second per area per energy) and a tunable photon energy. Synchrotron radiation is produced by charged particles travelling at relativistic speeds in magnetic fields, which force them to change trajectory.[108] This type of radiation is generated in storage rings by bending magnets, wigglers, or undulators, as represented in figure 2.8.

The field of the bending magnets accelerates electrons, and forces them into a circular path because an electron in a constant magnetic field is subjected to the Lorentz force. As a result, the electrons are forced to change trajectory and X-ray photons are emitted. Wigglers make the electron's trajectory a series of circular arcs. In other words, wigglers can be seen a series of bending magnets, and the intensity is enhanced proportional to the number of magnets in the wiggler. Undulators are an array of magnets that force electrons to oscillate in the horizontal plane due to an alternating magnetic field. The radiation emitted by those electrons interferes constructively; the resulting beam has a lower angular divergence with a narrow bandwidth, and the intensity is proportional to the square of the number of magnets in the undulator. The wavelength of the generated photons is controlled by tuning the magnetic field.

Figure 2.8 also shows other major components of a synchrotron ring. First, electrons are generated by an electron gun, then they run through a booster ring, where their energy is enhanced by a radio-frequency (RF) cavity. After that, electrons enter the synchrotron ring, which is supplied with bending magnets, undulators, wigglers, and focusing and defocusing mirrors (not represented here). Another RF cavity is present to compensate for the energy loss during the X-ray emission. X-rays are emitted tangentially to the ring and directed to a beamline. In some beamlines there is a monochromator tuned for a specific X-ray energy value to perform the experiment at the end

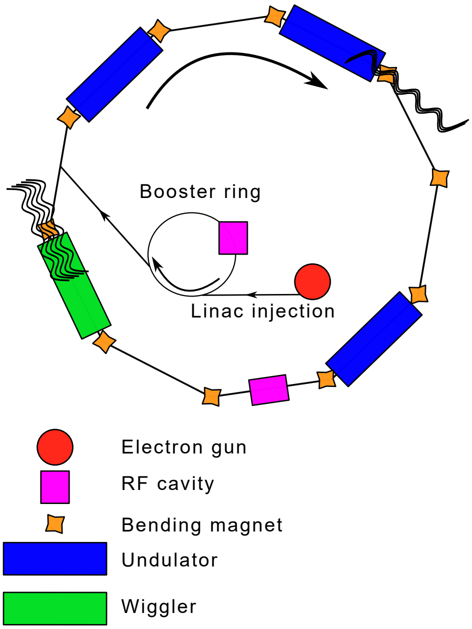

Figure 2.8: Schematic representation of a synchrotron ring.

station.

Experiments presented in this thesis were done at the Deutsches Elektronen-Synchrotron (DESY) in the Positron–Electron Tandem Ring Accelerator (PETRA III), which has an electron energy of 6.0 GeV and current of 100 mA (top-up mode).[109] The following two subsections will describe the end stations for beamlines P22 and P64 used in the research here.

2.2.3 POLARIS system for HP-XPS at beamline P22

P22 is a monochromatised beamline that generates a photon flux of $\approx 10^{13}$ photons per second under normal operation conditions.[110;111] Here, X-rays have an energy that can be tuned between 2.7 and 15 keV with both vertical and horizontal foci smaller than 10 µm. The beam divergence at the source is around 10 µrad, while the experimental divergence at the interaction point for usual measurements is lower than 0.4 mrad.

The POLARIS end station[112] was designed to operate at high pressures (beyond 1 bar) to perform XPS measurements. This end station consists of an experimental chamber, a hemispherical electron analyser (Scienta R4000) with a differentially pumped HiPP-2 electron lens, and a microchannel plate detector connected to a Basler CCD. A large hexapod allows the manipulation in the 3D space of the entire instrument.

For the measurements presented in this thesis, the hard X-ray regime was employed to study gold and oxygen core level regions. The advantage of using hard X-rays is that inelastic mean free paths (IMFP) of electrons become longer which helps working with high pressures in the chamber, nonetheless, the penetration depth of the beam increases which reduces the surface sensitivity. This surface sensitivity can be preserved by using a grazing incidence geometry, meaning the incident angle is below the critical angle for total external reflection. The incoming X-ray beam becomes evanescent inside the material and gets strongly damped in the bulk, thereby improving the surface sensitivity.[113] The usage of an X-ray beam with a high photon flux might cause beam-induced effects, meaning the X-ray beam could alter the surface chemistry under investigation by *e.g.* alteration of chemical bonds and/or locally heating the sample. Therefore, consecutive scans need to be collected at different photon fluxes to verify the possible presence of spectral changes during the chosen data acquisition time.

Another contrivance to be able to work with high pressures is to shorten the distance between the front cone (spectrometer inlet) and the sample, so it becomes close to the IMFP. This is achieved with a virtual cell: a circular symmetric gas inlet supplied by the front cone generates a micro-sized, pressurised gas cushion between the sample and the analyzer inlet. The directionality of reactant gasses prevents contaminants from the chamber walls from reaching the sample. With this configuration, sputtering and other surface science characterization techniques are also possible without transferring the sample. There are also some limitations from this design: high flows of pure gas are continuously pumped to keep high pressures and most of the gas is pumped away; and high flows shortens the residence time of reactants and products.

2.2.4 von Hamos-type geometry spectrometer for HERFD-XANES at beamline P64

P64 is a monochromatised beamline that generates a photon flux of $\approx 10^{13}$ photons per second under normal operation conditions.[114;115] Here, X-rays have an energy that can be tuned between 5 and 25 keV, which is within the hard X-ray regime. A von Hamos-type geometry spectrometer can be employed to perform both X-ray emission spectroscopy and high energy resolution fluorescence detected X-ray absorption near edge structure (HERFD-XANES).[116] The main components are the sample location, an analyser crystal array (with a von Hamos-type cylindrical bent geometry), and a detector positioning system. The sample holder is large enough to contain samples of different sizes, with an output window similar to the solid angle covered by the analyser crystals. The analyser crystal array consists of 8 crystal holders, where different silicon single crystals reflect fluorescence lines at different energy regions in the hard X-ray range. The detection system is at a selected Bragg reflection angle to the analyser crystal array, which allows detection of a specific fluorescence line. Two detectors, XSpectrum Lambda 750K and Dectris Pilatus 100K, are placed on a curved rail to position them at the proper Bragg angle, which varies from 85° to 50°. Their main difference is the pixel size which defines the energy resolution. The spectrometer works at atmospheric pressure, thus a polypropylene bag filled with helium is used to enhance the signal at the detector.

2.3 Electrochemical characterisation

This section provides a description of the electrochemical analytical techniques cyclic voltammetry (CV) and chronoamperometry (CA), followed by an illustration of the different types of ECs used in the research work presented in this thesis.

2.3.1 Electroanalytical chemistry

When electrodes are immersed in an electrolyte solution, there will be charge transport (CT) in the electrolyte and CT at the electrode/electrolyte interface. Different electroanalytic techniques are catalogued by these two phenomena. The research work presented in this thesis focuses on the electrode/electrolyte interface. There are two main categories of techniques to investigate the interface: static and dynamic. With static methods there is no current and no net reactions occur. The main example of a static technique is potentiometry, which consists of measuring the potential of an electrode relative to the potential of a reference electrode. In contrast, dynamic techniques do have net current and electron transfer. They are divided into two groups, depending on if the potential is controlled to specific values to measure a produced current, or the other way around. Here, attention is given to two controlled potential methods used in this thesis: cyclic voltammetry (CV) and chronoamperometry (CA).

A three-electrode cell is used for conducting both CV and CA measurements. The three electrodes are the working electrode (WE), the reference electrode (RE), and the counter electrode (CE); their connections shown in figure 2.9. The reactions under investigation take place at the WE. The RE has a known stable potential, therefore changes in the cell are due to the WE instead. REs are divided into aqueous reference electrodes, such as the standard hydrogen electrode (SHE) and Ag/AgCl electrode, and nonaqueous reference electrodes such as Ag/AgNO$_3$ in CH$_3$CN.[14] The position of the RE with respect to the WE is important to reduce the presence of Ohmic drop, which is the quantity of lost potential from the RE to the WE.[117] The Ohmic drop is due to Ohmic resistance, which depends not only on the distance between electrodes but also on the conductivity of the electrolyte. To keep the RE out of the circuit, so it can keep its constant potential, a CE is needed in this way the circuit is completed and charges can flow. The material for this electrode is usually inert so that it does not produce substances by electrolysis which could interfere with the reactions at the WE. The CE also needs to be much bigger than the WE one to ensure no current limitations arise.[118] In this way, the voltage of the WE with respect to a known reference potential can be measured with good accuracy. The potential is applied and controlled between the WE and CE by a potentiostat. When no potential/current is applied to the EC, the WE is at open circuit potential (OCP) relative to the RE. The potential at the WE is measured with respect to the potential of the RE.

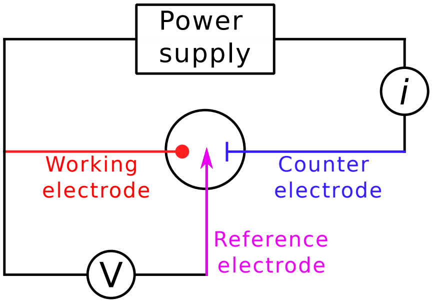

Figure 2.9: Typical representation of a three-electrode cell.

In CV, a range of potentials is scanned, and a current is created as a result of electron transfer between chemical species involved in electrochemical processes. The left side of figure 2.10 shows the triangular waveform of the potential for CV, where the potential is swept from E_1 to E_2 and then back to the starting value. The final outcome is an I-E curve, represented on the right side of figure 2.10 and mathematically explained by the following equations:[119]

$$i_{forw.} = kc(1-\theta)exp[\beta(E \pm st)F/RT] \tag{2.16}$$

$$i_{back.} = kc\theta exp[-(1-\beta)(E \pm st)F/RT] \tag{2.17}$$

where k is an equilibrium constant, c is the concentration of the adspecies in the electrolyte solution, θ is the occupied-site fraction, β is a barrier symmetry factor, $E \pm st$ is the time-variant potential with s the rate of modulation in Vs^{-1}, F is the Faraday constant, R is the universal gas constant, and T is the temperature. This curve is related to the chemical processes happening on the surface of WE with kinetics relative to the timescale of the sweep, as shown by the current flow.[120] The forward peak describes an oxidation reaction, while the backward peak describes a reduction reaction. When the peaks are symmetric the whole system undergoes reversible reactions.

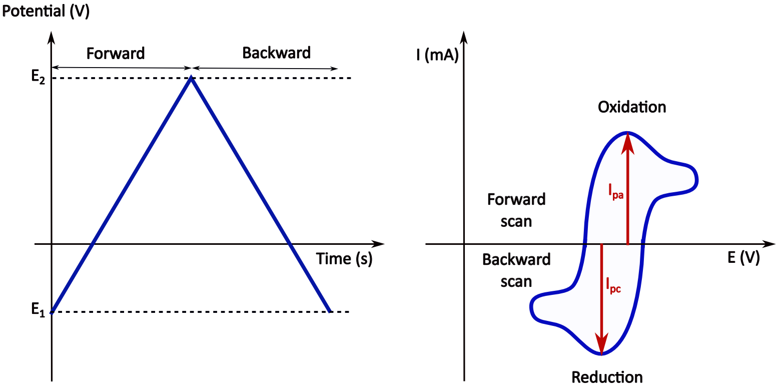

Figure 2.10: ***Left*** - Cyclic potential sweep; ***Right*** - Resulting cyclic voltammogram.

The variation of the sweep rate (mV/s) affects the shape of the curve. A slow scan lets the diffusion layer grow more than a fast scan; as a consequence, at the surface of the electrode the flux is smaller in a slow scan which leads to lower currents.[12;121] However, lower sweep rates give a better resolution of different process (sharper peaks) because of a higher probability of the products to be in equilibrium with the electrode potentials and being detected. The peaks in a CV are the currents for anodic (oxidation) and cathodic (reduction) processes (I_{pa} and I_{pc}), respectively.

In CA, the potential is applied in steps to measure the current generated during redox processes. Figure 2.11 summarises the basis of CA. The starting point of the measurement is the analyte which has not been subjected to redox reactions, at potential E_1. Then, this analyte is brought to a potential (E_2) where it undergoes these chemical processes (left side on figure 2.11). From this, a diffusion-controlled current is plotted as a function of time, depicted on the right side of figure 2.11, which is mathematically described by Cottrell equation:

$$i_d(t) = \frac{nFAD_o^{1/2}C_o^*}{\pi^{1/2}t^{1/2}} \tag{2.18}$$

where n is the number of electrons to reduce/oxidize one molecule of analyte, F is the Faraday constant, A is the area of the electrode, D_o is the diffusion coefficient for species in the analyte, C_o^* is the initial concentration of the reducible analyte, and t is time.

The electroanalytic techniques introduced in this section provide ways to quantify concentrations of reaction products and to perform kinetic analysis to interpret reaction mechanisms. The main drawback is that they are not very suitable for the *identification* of unknown species, like reaction intermediates and products; for that we use spectroscopic techniques. The union of spectroscopy and electrochemistry, known as spectroelectrochemistry

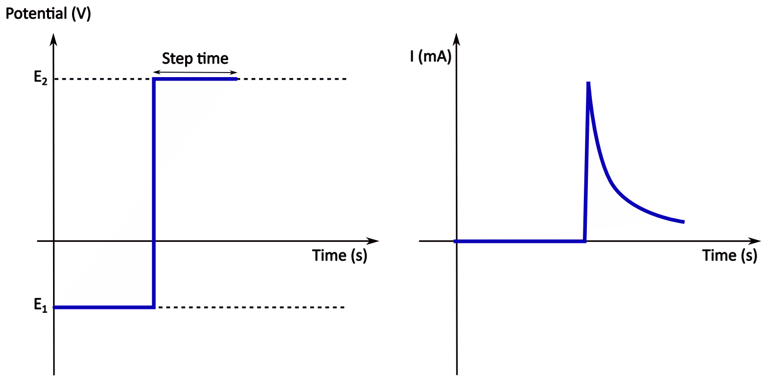

Figure 2.11: ***Left*** - Potential applied to the cell as a function of time; ***Right*** - Current vs. time.

(SPEC), overcomes this issue. It is commonly accepted that this field was started by the work of T. Kuwana *et al.* in 1964.[122] Since then, the combination of these two fields has found broad space in research. Some examples of spectroscopic techniques used in SPEC are: absorption spectroscopy (from the IR to the X-ray region), Raman scattering spectroscopy, and magnetic resonance techniques.[123] **Papers I, II, and III** are based on spectroelectrochemical methods (SFG, XAS, and XPS).

2.3.2 Electrochemical cell for SFG spectroscopy

For **Papers I and II**, a custom thin layer EC was designed from the work of Tong et al.[124] Figure 2.12 shows its different parts with the mounting steps. The internal section consists of a CaF_2 window (Ø 25 mm x 2 mm, both sides optically polished) on top of a quartz substrate (Infrasil 302, Ø 45 mm x 2 mm). Three gold electrodes are deposited on the quartz plate using photolithography. Figure 2.12.a shows the electrode structure after this procedure and their roles in the measurements. The diameter of the centre circle (WE) is 5.80 mm, the area immersed in the electrolyte is around 1.30 cm^2, and the space between the WE and CE is 0.6 mm. The centre part of the three electrodes creates a circle with the same diameter as the CaF_2 window. A Teflon spacer of thickness 25 µm is between the CaF_2 window and the quartz substrate to fix the volume of the electrolyte solution, which is around 3.5 µl. The electrolyte solution is injected by a tubing system through two holes in the CaF_2 window. The liquid flow is controlled by a peristaltic pump (Ismatec Reglo ICC, soft-wall tube ID 0.64 mm Tygon Chemical, and PFA tube with ID 0.51 mm). Internal O-rings in the EC prevent leakage. Surrounding polyether ether ketone (PEEK) plates constrain these components, which are pressed by six screws. There is a slit in the top PEEK plate to let light strike the WE. Electrodes are connected to a potentiostat (Bio-Logic SP 200) by gold foils, which are pressed by the PEEK plates.

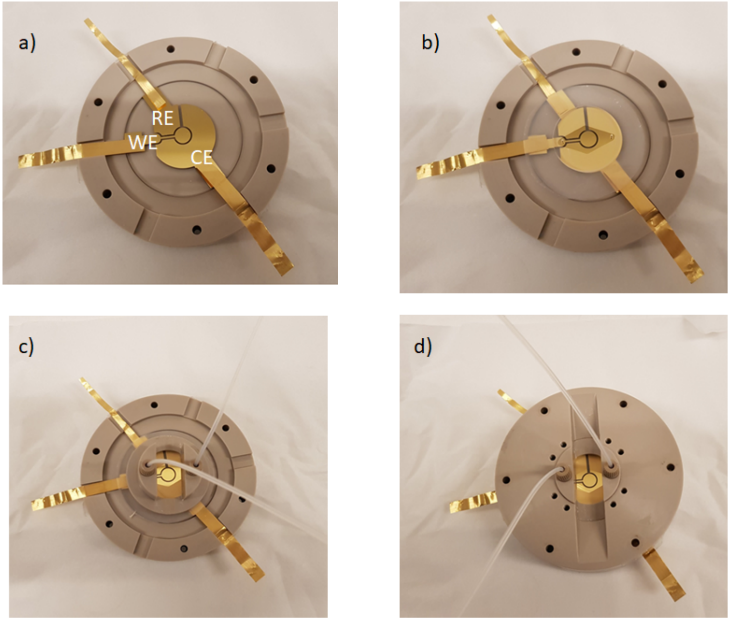

Figure 2.12: EC configuration: a) bottom PEEK plate with the electrodes and the electrochemical connections, b) Teflon spacer and CaF_2 window are added in this order, c) central PEEK component for the electrolyte flow in the cell is located on top, d) top view of the fully mounted cell.

2.3.3 Electrochemical cells for X-ray spectroscopies

Two different ECs were used for the HP-XPS and HERFD-XANES measurements presented here. The sample holder for HP-XPS (**Paper III**) is shown in figure 2.13. It is made of PEEK and has an L-shape to be placed on a stage equipped with motors to control its position in the 3D space. The WE is 100-nm gold film on top of 10 nm of titanium, which was used as adhesion layer. The RE is a gold wire, and the CE is a platinum foil. The electrical connections are copper wires and rods. The dip-and-pull method was employed.[125] The first step of this technique is to dip the electrodes in a beaker (Starna Scientific LTD) containing the electrolyte (1 M H_3PO_4) and to execute the electrochemical treatments with a Bio-Logic SP200 potentiostat. Then, the electrodes are pulled up while keeping their bottom part in the electrolyte to create a thin liquid film on the surface in order to alter the oxidation as little as possible when XPS spectra are collected. The electrolyte was degassed before being inside the chamber.

Figure 2.14 depicts a schematic overview of the EC used for HERFD-

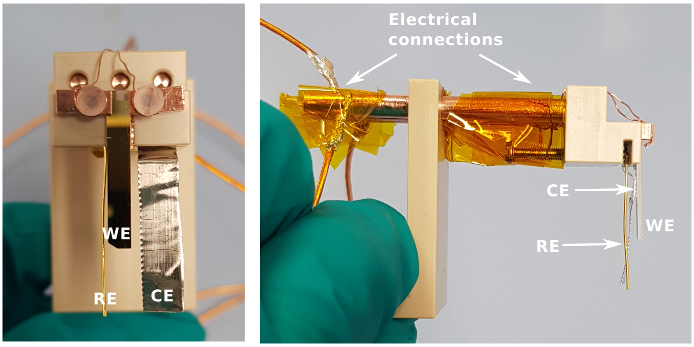

Figure 2.13: Overview of the sample holder for the EC used in HP-XPS measurements.

XANES measurements in **Paper III**. It is a custom-made single compartment cell made of PEEK with a gold thin film (around 5 nm) sputtered onto a graphene sheet as WE, saturated calomel electrode (SCE, KCl saturated) as RE, and a platinum mesh as CE. There is an aperture on one side of the EC to let nitrogen in to saturate the electrolyte ($HClO_4$, 1 M). For HERFD-XANES, the EC was located at an angle of around 45° with respect to the surface normal, and the incident X-ray beam interacts from the back of the WE.

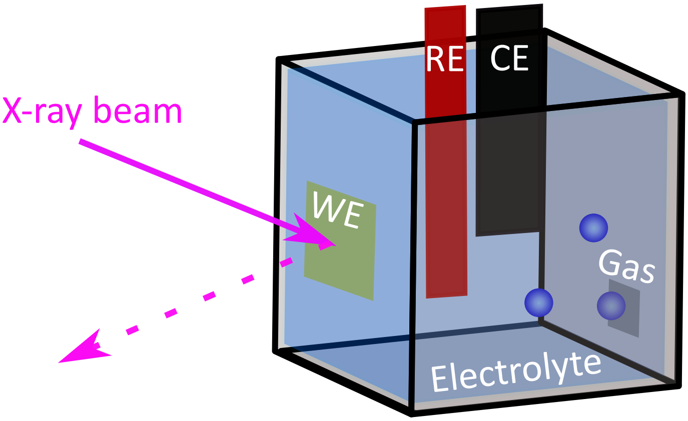

Figure 2.14: Overview of the EC used in HERFD-XANES measurements. The X-ray beam interacts from the back side of the sample (WE).

2.3.4 Preparation of gold electrodes for spectroelectrochemical measurements

The gold electrodes for SFG measurements have a more complicated preparation than the other electrodes because a specific shape was needed. The electrodes are composed of gold (200 nm) on top of titanium (10 nm), the shapes of which are shown in figure 2.12. Titanium was chosen as adhesion layer for its good stability in large anodic potential ranges.[126] The electrodes are fabricated using photolithography and the double layer resist lift-off technique. A quartzglass window (Infrasil 302 ø, 45±0.1 mm x 2±0.1 mm optically polished from Korth Kristalle GmbH) is first cleaned using ultrasonic frequencies with a solution of methanol in Milli-Q water (1:1) in an ultrasonicator for 30 minutes. Then, the substrate undergoes a deeper cleaning with a strong O_2 plasma (10 W RF bias, 250 W RF to ICP (inductively coupled plasma) generator, p=95 mTorr) for 5 minutes. 500 nm of lift off resist (LOR7B) are deposited by spin coating (1 minute at 4500 rpm), and soft-baked on a hot plate for 2 minutes at 190 °C. Spin coating is repeated to deposit 1500 nm of positive photoresist (Microposit S1813) for 1 minute at 4000 rpm, followed by soft-baking on a hot plate for 1 minute at 100 °C. The substrate is exposed to blue light using a maskless photolithography tool, and the pattern is developed in an MF-319 developer for 30 seconds. After this, the surface is cleaned in soft O_2 plasma (10 W RF bias, 50 W RF ICP generator, p=95 mTorr) for 8 minutes. A titanium layer of 10 nm followed by a gold layer of 200 nm are then deposided in a single vacuum cycle by electron beam evaporation. The electrodes are lifted off in mr-Rem 700 remover overnight to eliminate LOR7B and Microposit S1813. Then a final cleaning in a strong O_2 plasma (10 W RF bias, 250 W RF ICP generator, p=95 mTorr) is done for 3 minutes.

For HP-XPS measurements, the WE consisted of gold (thickness 100 nm) on titanium (10 nm) was deposited in a similar way as for the electrodes for SFG measurements. The support was silicon or quartz chip (3 mm x 20 mm, thickness 1 mm) and figure 2.13 shows the electrode at the end of the preparation. For HERFD-XANES measurements, the WE was a gold thin film (thickness ~ 5 nm) prepared by DC sputtering of Au at 5 mTorr Ar pressure and 20 W onto graphene sheets (thickness 25 μm). Figure 2.14 depicts the final outcome.

2.3.5 Calibration of the gold reference electrode

Before doing electrochemical measurements, the behaviour of gold as reference electrode was investigated since it belongs to the category of quasi-reference electrode (QRE). This means that its potential does not change during measurements but it is unknown, therefore a calibration with a true reference electrode must be done. This consists of recording CVs of a calibrating redox couple first versus the QRE and then versus a true RE in the same conditions. The chosen internal standard is potassium ferricyanide ($K_3[Fe(CN)_6]$), which is very common in literature since the oxidation of ferrocyanide ion $(Fe(CN)_6)^{4-}$ into ferricyanide ion $(Fe(CN)_6)^{3-}$ is fast and reversible in several solvents.[14;127] The Ag/AgCl electrode in saturated KCl was chosen as true RE, and a 0.5 M of potassium ferricyanide solution was added in 1 M of H_3PO_4 (pH 1), same pH used for the experimental investigations. The measurements shown in figure 2.15 were done using gold wires in a beaker due to the design of the thin layer EC, which does not allow using the available Ag/AgCl. The same behaviour for gold wires (bulk electrolyte) and gold deposited on a quartz plate (thin-film electrolyte) was observed from the CVs. Figure 2.15 shows the CVs recorded with the gold RE (red curve) together with the ones with Ag/AgCl (orange curve). The yellow and orange vertical lines represent the mean potential ($E_{1/2}$) between the currents of the cathodic and anodic processes for both curves, also called formal potential.[14] Applying the Ag/AgCl to SHE shift, the voltage difference between gold RE and SHE is found to be about 0.7 V.

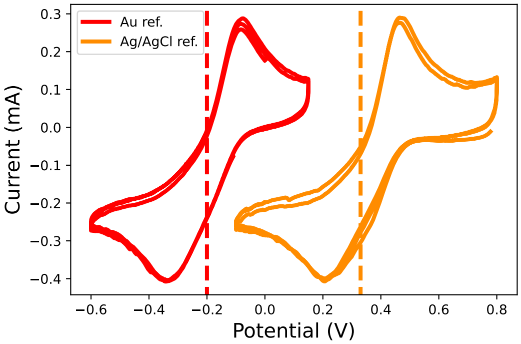

Figure 2.15: Comparison between Au RE and Ag/AgCl RE in presence of potassium ferricyanide in 1 M H_3PO_4. CV scan rate: 100 mV/s.

2.4 Mass spectrometry

Mass spectrometry (MS) is used to measure the mass of chemical species after being ionised. A typical spectrum represents the abundance of the generated ions as a function of their mass-to-charge ratio (m/z), which is the ion mass (m) divided by the charge (z) of the ion. The discovery of isotopes by J. J. Thomson and his student F. W. Aston in 1913 set the basis for the development of MS. Thomson and Aston together built the first mass spectrometer, the importance of which was immediately recognised as it was used in the research on isotopes in the Manhattan Project.

The main components of a mass spectrometer are an ioniser, a mass filter, and a detector, which are sketched in figure 2.16. In **Paper IV** an SRS CIS300 mass spectrometer was used, where the ioniser is a heated tungsten filament which generates electrons. These electrons are accelerated towards a positively-charged anode and strike the sample molecules to ionise them.

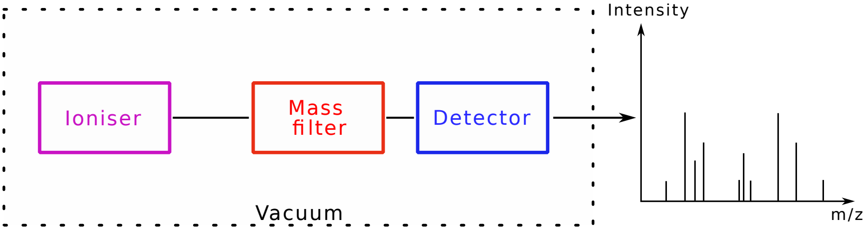

Figure 2.16: Schematic sketch of a mass spectrometer showing the main components (ioniser, mass filter, and detector) and a representation of a conventional spectrum is also included.

The mass filter separates the ions based on their *m/z* ratio, and an electric field controls the trajectory of those ions. In the SRS CIS300, a quadrupole mass filter is used, which has two pairs of cylindrical rods with opposite signs parallel to one another. The working principle of which is depicted in figure 2.17: between the two pairs of rods, an electrical voltage is applied which has a combination of DC (U) and RF (V_0) voltages. One pair of rods (in the X-Z plane) is connected to a positive DC voltage with a superimposed sinusoidal RF voltage, while the other pair of rods (in the Y-Z plane) is connected to a negative DC voltage with a superimposed sinusoidal RF voltage 180° out of phase with the first RF voltage. Ions with a lower *m/z* ratio gain energy from the field in the X direction, since they are in phase with the RF component, and their oscillatory amplitude increases until they reach the rod and get discharged, hence only ions with higher masses are transmitted to the end of the quadrupole to be detected. Heavier ions are unstable along the Y direction due to the defocusing effect of the DC component, hence only ions with lower masses are transmitted to the other side of the quadrupole and detected. The selectivity of the mass filter is given by the DC/RF ratio: increasing DC wile keeping RF constant defocuses heavier ions by the negative DC component.

Once the ions pass the quadrupole, they reach a detector which consists of four macro multi-channel continuous dynode electron multipliers with a cone attached to the front end. A potential bias on the cone accelerates these ions towards it. Ions striking the cone at high velocities generate secondary electrons by secondary electron emission. The number of secondary electrons is enhanced by multiple accelerations which yields even more secondary electrons. The current generated by the secondary electrons is proportional to the abundance of the initial ion current.

A calibration is usually needed to obtain information about the quan-

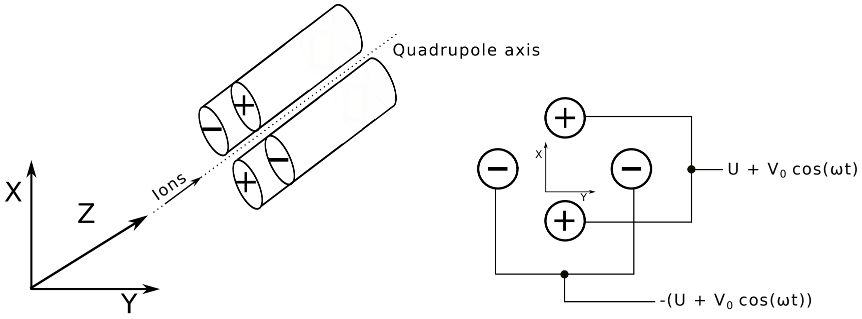

Figure 2.17: Schematic sketch of a quadrupole mass filter with its connections. *U* is the amplitude of the DC voltage applied to either pair of rods, V_0 is the amplitude of the RF voltage applied to either pair of rods, ω is the angular frequency of the RF.

tities of reaction products from analytical characterisations such as MS. In **Paper IV**, a calibration was done using a constant amount of krypton (^{86}Kr) while the concentration of CO_2 and H_2 were changed within a selected range. Krypton was chosen as an internal standard because it does not participate in the chemical reaction being investigated. A linear calibration curve was calculated after normalising the areas of CO_2 (m/z= 44) and H_2 (m/z= 2) for the different concentrations with the area of the m/z = 86 signal corresponding to ^{86}Kr. This calibration curve is used to calculate the amount of the reaction products. A baseline correction was done by subtracting a blank spectrum, collected without the catalyst, from the spectrum after using catalyst.

3. Summary of results

This chapter summarises the results of the articles at the beginning of the thesis. **Paper I** focuses on the change of electronic structure of gold film due to gold oxide remnants after electrochemically-formed oxide-derived gold (OD-Au) is created from gold films. Additional investigation, both theoretical and experimental, was done to better understand the change of electronic structure and chemical composition of gold films after their oxidation in acidic media (**Papers II and III**). **Paper IV** deals with heterogeneous catalytic studies of CO oxidation by gold nanoparticles supported on metal oxides, with emphasis given to how water participates in this process.

3.1 Study of electrochemically-formed oxide-derived gold from gold films

As discussed in Section 1.2.3, OD-Au materials are created by reducing an oxide precursor, and present enhanced catalytic properties for CO_2 reduction to CO compared to pure gold metal. Consensus to explain these improved properties has not been reached yet. **Paper I** aims to provide more information on how the surface changes from gold metal film to OD-Au by using two different electrochemical protocols together with *operando* SFG and *ex situ* HP-XPS measurements.

Figure 3.1 shows the combined CV (blue) and *operando* SFG (orange) measurements of gold surface in acidic aqueous conditions (H_3PO_4, pH 1) for different potential ranges versus the standard hydrogen electrode (SHE) reference electrode. The electrochemical protocol consists of an electrochemical annealing at 0.7 V for 30 seconds, followed by a CV cycle with a range from 0.7 V up to a potential value in 1.5-2.5 V. The CV measurements are in agreement with literature,[35;38] and the following regions are observed:

- region *Ia* (0.70–1.25 V): double-layer charging/pre-oxide formation;
- region *IIa* (1.25–1.45 V): thin precursor of compact oxide formation;
- region *IIIa* (1.45–1.80 V): compact oxide growth;
- region *IVa* (> 1.80 V): hydrous oxide growth and the OER,
- region *Ic*: for the change of the sweep direction which lowers the OER condition;

- regions *IIc* (≈ 0.90–1.25 V) and *IIIc* (< 0.90 V): reduction of compact and hydrous oxide.

The variation of the SFG signal in figure 3.1a resembles the one observed in the near-infrared during second harmonic generation (SHG, degenerate form of SFG),[128–130] and follows the formation (region *IIa*) and reduction (region *IIc*) of an initial thin oxide overlayer, the formation of the oxide decreases the free electron density on the gold surface. The SFG signal gets the original intensity back at the end of the CV scan, in which it is metallic in the double layer charging region/pre-oxide formation region (*Ia* and *IIIc*). By increasing the anodic potential, new SFG features appear (figure 3.1 a-e, CV scan rate 10 mV/s), which depend on the CV scan rate (figure 3.1 f, CV scan rate 50 mV/s): the beginning and ending SFG intensities of the CV cycle do not overlap (*SFG loss*); and the SFG intensity has a linear decrease as a function of the potentials in regions IIIa-IVa (*SFG drop*: reduction of the SFG intensity at the upper CV positive potential).

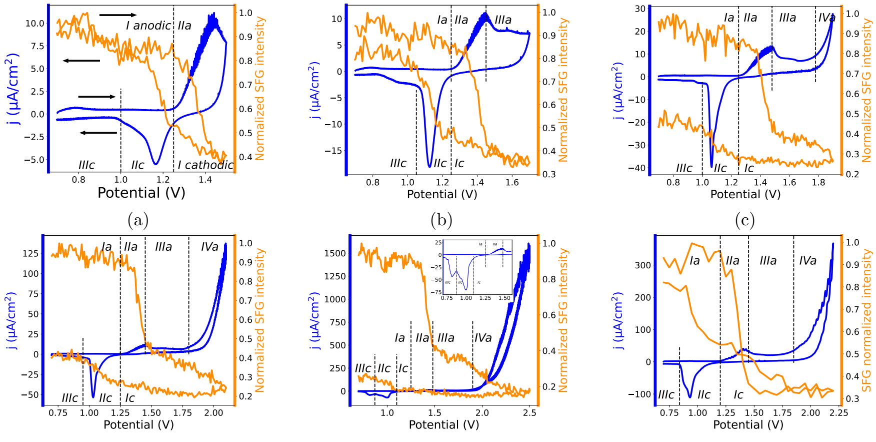

(a) (b) (c)

(d) (e) (f)

Figure 3.1: (a-e) Combined SFG (orange) and CV (blue, scan rate 10 mV/s, potentials vs. SHE) measurements of gold in H_3PO_4 (pH= 1) for different upper potentials, the lower potential is 0.7 V for all measurements. The Roman numerals with **a** and **c** mean anodic and cathodic, respectively, and indicate different regions of oxidation and reduction. More precisely, region *Ia* for the double-layer charging/pre-oxide formation, region *IIa* for the thin precursor of compact oxide formation, region *IIIa* for the compact oxide growth, and *IVa* for hydrous oxide growth and the OER, region *Ic* for the change of the sweep direction which lowers the OER condition, and regions *IIc* and *IIIc* for the reduction of compact and hydrous oxide. The black arrows in (a) indicate the potential and SFG scanning directions. In (e) an inset shows a zoomed-in portion (x3) of the reduction part of the CV. (f) Combined SFG (orange) and CV (blue, scan rate 50 mV/s, potentials vs. SHE) measurements of gold in H_3PO_4 (pH= 1). Reproduced from **Paper I**.

As the data show, the presence of both *SFG drop* and the *SFG loss* in the multi-layer oxide growth in regions IIIa–IVa indicates a slow oxidation process that decreases the metallic SFG response. It seems that the OER (region IVa, figures 3.1c-e) at slow scan rate does not significantly affect the SFG signal. Hence, it could be that the SFG variation is connected to the higher influence of oxygen at oxide/metal interface, as the other oxide multilayers are too far from the interface to affect the SFG signal. However, stronger anodic conditions cause *SFG loss* even if the surface oxide is reduced as shown from the CV measurements (figure 3.1).

Fixed potentials (CA) can also be employed for the OD-Au preparation. This second electrochemical protocol, starting from a clean gold surface, consists of:

- an oxidation step, ranging from 0.7 V to 2.5 V, is held for 30 seconds;
- a reduction step is held at 0.7 V for 10 seconds;.
- a surface characterization, CV (range 0.7–1.5 V) together with SFG measurements were done simultaneously as in figure 3.1.a.

In figure 3.2.a the CV scans are very similar for the duration of the analysis indicating that the same available metallic surface sites, and same electrochemical processes at the surface, as in figure 3.1a. It is only when the first step of this protocol is 2.5 V, that the CV manifests different cathodic behaviour at the end of the scan, which suggests the presence of hydrous oxide which is not fully reduced, [35] but this does not affect the SFG response. At the same time, the SFG intensities in figure 3.2.c are also consistent with a metallic surface as seen in figure 3.1.a, with an *SFG drop* of about 50–60% and no *SFG loss*, which is consistent with the incipient oxide formation and its reduction from an initially-metallic surface.

Interestingly, there is a decrease of the overall SFG intensity for a preparation voltage (CA) higher than 1.5 V (figures 3.2.b-c). A possible explanation is the presence of oxygen atoms below the surface but close enough to it to change the surface free electron density. Surprisingly, among all the SFG intensities, the lowest one is for the CA at 0.9 V (point 8, after the preparation at 2.2 V), though further oxidation is not expected at this potential and the corresponding CV is consistent with figure 3.2a. A rearrangement of the pre-existing surface gold oxide might be present, which was not completely removed during step 1 (0.9 V). Preparing the surface by applying 0.5 V provides almost full recovery, as the trapped oxygen is relaxed giving an electron distribution close to the one at the beginning of this second protocol.

Considering both OD-Au preparation protocols in **Paper I**, the gold oxide was reduced at different rates. It has been shown that low rates (like figure 3.1) favours diffusion of gold ions to the bulk electrolyte during oxidation, and only little redeposition of dissolved gold occurs during reduction. [29;131;132]

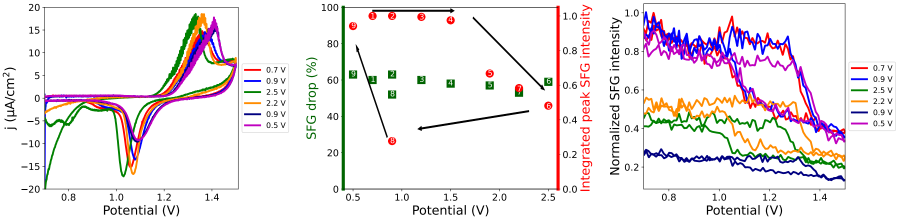

(a) (b) (c)

Figure 3.2: (a) CVs (range 0.7–1.5 V vs. SHE, scan rate 10 mV/s) after doing the second electrochemical protocol. The legend and the black arrows shows the chronological order of some CA measurements from step 1. (b) Green squares: *SFG drop* collected after the chosen potentials in step 1 (across the full data set) are applied. Red circles: normalized SFG intensity at the end of the CVs; the normalization is to the SFG intensity when step 1 is 0.7 V (neat gold surface). The numbers (1-9) indicate the chronological order of the measurements. The x-axis indicates the CA potential in step 1 of the protocol. (c) Integrated potential-dependent SFG intensities collected during step 3 of the protocol. The normalization is done with respect to the SFG intensity from a neat gold surface (red curve, 0.7 V vs. SHE). The legend shows the chronological order of selected CA measurements vs. SHE during step 1. Reproduced from **Paper I**.

This leads to the creation of a not well-protected subsurface oxide by the new surface gold atoms, which can be easily removed by additional electrical treatments. But, when the reduction rate is high as during CAs (in our case figure 3.2), more gold is redeposited back on the electrode surface and almost gold is present in the electrolyte.[132] This provides better protection for the oxide remnants in the subsurface and necessitating more time to release them. Currently, however, detailed mechanisms are lacking.

To further test the subsurface oxygen hypothesis, *ex situ* HP-XPS is used to examine metallic gold, oxidised gold (figure 3.3, grazing incidence angle 0.2°), and OD-Au (figure 3.4) created using similar electrochemical conditions as in figure 3.2). A saturation of water vapour was present in the chamber during measurements to preclude the gold (hydr-)oxide from getting reduced by the vacuum. Figure 3.3 shows XPS spectra of the gold surface before (figures 3.3.c–d) and after oxidation (figures 3.3.a–b), which was done by (i) CA at 0.7 V for 20 seconds, (ii) CV between 0.7 V and 2.2 V with a scan rate of 10 mV/s, and (iii) CA at 2.5 V for 50 seconds. In the Au 4f core-level region (figure 3.3.c), the metallic surface has the characteristic 5/2 and 7/2 spin-orbit components with the intensity branching ratio of 3:4. For the oxidized electrode (figure 3.3.a), two additional intensities are identified after a deconvolution analysis by using the same spin-orbit split as the metallic gold, indicating the presence of Au(III) (85.6 and 89.9 eV).[32;33;133–137]

In figure 3.3.d, only a water signal, adsorbed or multilayer, is detected in the O 1*s* region when gold is metallic. For the oxidised gold (figure 3.3.b),

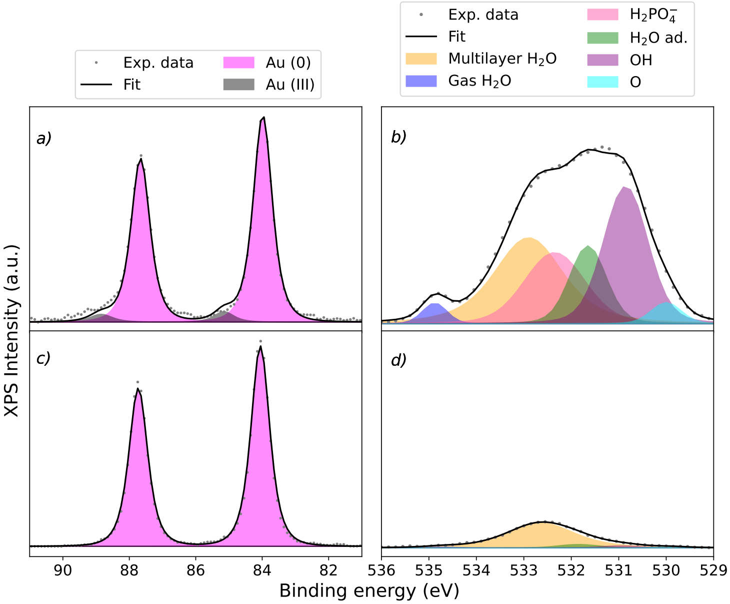

Figure 3.3: HP-XPS spectra for Au 4f (a and c) and O 1s (b and d). hν = 7000 eV, grazing incidence angle 0.2°. Bottom (c and d): before oxidation. Top (a and b): after electrochemical treatment (CA at 0.7 V for 20 second, CV between 0.7 and 2.2 V with a scan rate of 10 mV/s, and CA at 2.5 V for 50 seconds). Reproduced from **Paper I**.

after peak deconvolution, more components are present: oxide (~530.0 eV), hydroxide (~531.0 eV), adsorbed water (~531.8 eV), dihydrogen phosphate ($H_2PO_4{}^-$)(~532.5 eV), multilayer water (~532.5 eV), and gas-phase water.[53;92;138;139] This is consistent with what observed in figure 3.3.a. The main chemical compositions which have been suggested for Au(III) are Au_2O_3 and $Au(OH)_3$.[32;35;36]

The OD-Au was prepared in similar conditions as in figure 3.2.b point 6: (i) CA at 0.7 V for 20 seconds, (ii) CV from 0.7 V to 2.2 V with a scan rate of 10 mV/s, (iii) CA at 2.5 V for 50 seconds, and (iv) CA at 0.7 V for 25 seconds. During the last step no current is present, proving that the surface is metallic from an electrochemical point of view. The HP-XPS spectra of OD-Au (figures 3.4.a–b) were collected with a higher grazing incidence angle (0.5°) to examine oxide species further below the surface after OD-Au is formed. Small shoulders are visible at 85.6 and 89.9 eV in the Au 4*f* region of OD-Au (figure 3.4.a) compared to pure metallic gold, which indicate spin-orbit components of gold in oxidation state +3.

Using the same peak deconvolution model as for the oxidised gold surface, the oxide and hydroxide species for OD-Au (figure 3.4.b) have an oxide-to-hydroxide ratio of 0.10, which is smaller than the ratio from figure 3.3.b of

0.36. This indicates that the Au_2O_3 is more stable than $Au(OH)_3$ when OD-Au is formed. The Au_2O_3 seems to be located below a layer of metallic gold, since the CA indicates a metallic surface at the end of the OD-Au formation.

Both SFG and HP-XPS data support the presence of (hydro-)oxide remnants in OD-Au even if the corresponding electrochemical measurements suggest that the surface is fully reduced, *i.e.* metallic, when OD-Au are formed. These subsurface remnants affect the SFG signal thorough changes of the surface electronic structure. The XPS spectra suggest these remnants in OD-Au to be Au_2O_3 and $Au(OH)_3$. Knowing that oxide remnants are formed in Au-OD may help in building a better understanding of the improved catalytic properties OD-Au with respect to pure metallic gold.

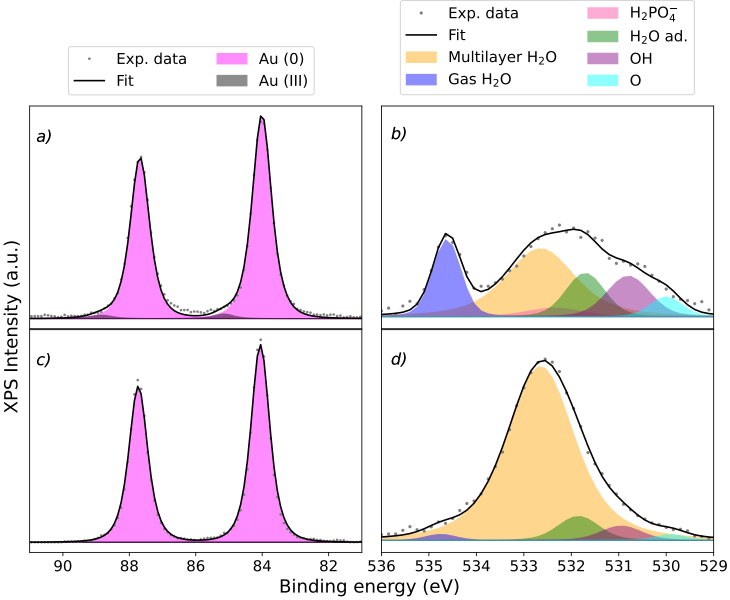

Figure 3.4: HP-XPS spectra for Au 4f (a and c) and O 1s (b and d). hν = 7000 eV, grazing incidence angle 0.5°. Bottom (c and d): before electrochemical treatment; Top (a and b): OD-Au electrochemical treatment (CA at 0.7 V for 30 second, linear sweep voltammetry from 0.7 to 2.5 V with a scan rate of 10 mV/s, CA at 2.5 V for 50 seconds, and CA at 0.7 V for 25 seconds). Reproduced from **Paper I**.

3.2 Models for electro-oxidation and nonlinear optical response of gold surfaces

After conducting a fully-experimental study in **Paper I**, theoretical calculations were done to model both the electrochemical and SFG responses together from gold surfaces during an anodic linear sweep, since they are usually considered separately. The electrochemical model consists of a two-step process: a rapid reversible chemisorption of oxygen (O_{ad}), followed by a slower irreversible place exchange of gold atoms with O_{ad}. This place exchange reverses the local dipole orientation moving the system away from equilibrium, allowing oxide growth. These calculations are based on the work of Marshall and Conway [140–143] and Furuya *et al.* [144] The SFG response was modelled following the work of Maytorena *et al.* [77] which has been further elaborated upon by Busson and Dalstein. [78;79;145] In this model, the electron density is given by the sum of a free electron gas and a bound electron density. The electron density spillover at the surface is considered to be only due to the free electrons.

In figure 3.5, computed linear sweep voltammetry (LSV) and SFG responses from the surface of gold are compared to experimental measurements for a potential range of 0.7–1.9 V vs. SHE. In this study, the LSV measurements correspond to the anodic part of a CV. Our model works well for both LSV and SFG until 1.4 V; after that, although the SFG remains in good agreement with experiment, the LSV current does not match the experimental data. A possible explanation for the lack of agreement between theoretical and experimental LSV curves could be that a different mechanism process is present from 1.4 V on; Au_2O_3 formation has been suggested, [35] which is not part of the present model.

Figure 3.6 shows the corresponding calculated charge densities for the gold metal surface (σ_m), adsorbed charges (σ_{ad}), water polarization (σ_w), and place-exchange (σ_{pe}). At 1.2–1.3 V, σ_{ad} changes, which makes σ_m increase. At 1.3–1.4 V, the rapid variation of σ_{ad} together with the variation of σ_w makes σ_m increase rapidly. The progressive change of σ_{ad} at potentials above 1.4 V is mirrored by σ_m.

In light of the information from figure 3.6, the reduction of SFG intensity at potentials below 1.3 V in figure 3.5 seems related to the variation of σ_w; in other words, polarisation of adsorbed water enhances the electric field on the surface.

The rapid drop in SFG intensity happens with the main oxygen adsorption around 1.4 V (figure 3.5); the corresponding increase of σ_{ad} (figure 3.6) leads to a change of σ_m together with an increase of σ_w. These changes in σ_m and σ_{ad} make bound and free surface electron densities change through the corresponding dielectric function, resulting in a variation of the nonlinear optical response via the effective surface second order susceptibility (χ^{eff}).

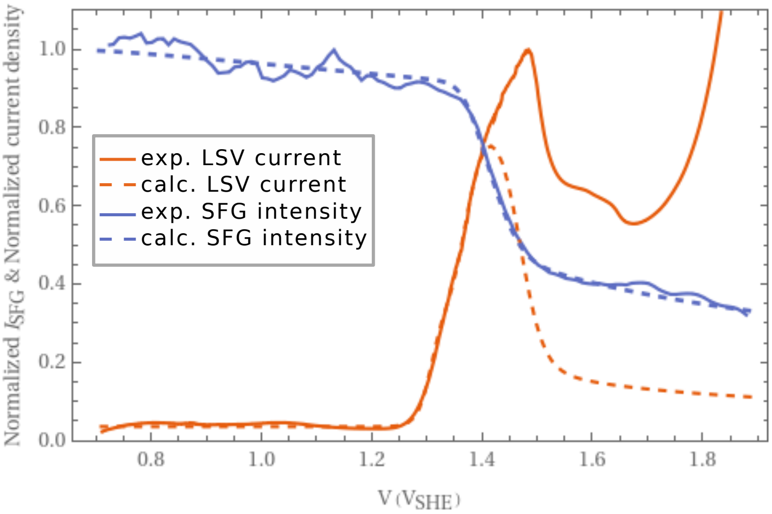

Figure 3.5: LSV current (solid, red) and SFG intensity (solid, blue) normalized at 1.48 V and 0.7 V vs. SHE, respectively, together with the corresponding calculated curves based on the model fit (dashed). Reproduced from **Paper II**.

After the rapid SFG intensity variation in the oxygen pseudo-equilibrium adsorption peak (about 1.5 V), the SFG intensity has a linear decrease. Figure 3.5 shows that the oxidation growth continues (shown by the experimental LSV curve), but this only partially seems to be due to the changes in σ_{ad}. This indicates that the main oxide growth does not block the sites for the oxygen adsorption process, nor prevents the water from reach those sites. The multilayer oxide growth could be seen as a not-dense 3D structure, suggesting a similar conclusion to that of Conway *et al.*[41] who hypothesised island formation during the monolayer growth, provided that these islands are centres for 3D oxide growth.

The main feature from the nonlinear optical response that has been observed is the rapid change of intensity at the main quasi-equilibrium adsorption range (1.3–1.5 V vs. SHE) at various wavelengths.[129;130;146] When the fundamental wavelength is in the IR range, the behaviour is as shown in figure 3.5, but the response is reversed when the fundamental wavelength is 532 nm (18800 cm^{-1}).[128] This behaviour was investigated with our model. Figure 3.7 shows the calculated relative change in nonlinear response ($\Delta I^{ad}_{SFG/SHG}$) versus the final light frequency corresponding to incident frequencies from the near-infrared to ultraviolet. For SFG, one wavelength was kept at 800 nm (12500 cm^{-1}). Here, the relative change is the difference of the of $I^{ad}_{SFG/SHG}$ at the beginning and ending edges of the rapid decline, normalised by the intensity at 0.575 V vs. SHE. These edges are at 1.36 and 1.46 V, respectively.

At low frequencies in figure 3.7, where the free electron contribution

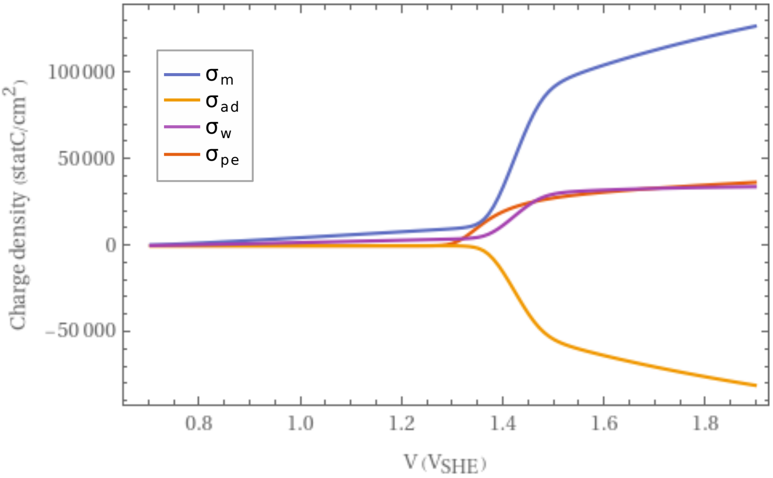

Figure 3.6: Calculated charge densities for the gold metal surface (σ_m, blue), adsorbed charges (σ_{ad}, yellow), water polarization (σ_w, purple), and place exchange (σ_{pe}, red) for a potential range of 0.7–1.9 V vs. SHE. Reproduced from **Paper II**.

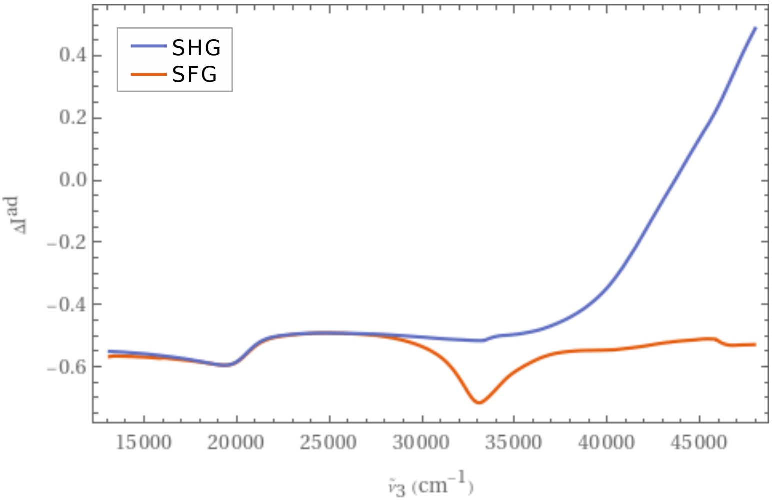

Figure 3.7: Calculated relative change in nonlinear optical response in the main quasi-equilibrium adsorption range, V=1.3-1.5 V vs. SHE, as a function of sum frequency for SHG (blue) and SFG with one wavelength fixed at 800 nm (orange). The small features at 33000 cm^{-1} and 46000 cm^{-1} in the SHG and SFG data, respectively, are spurious, caused by a small mismatch of the two combined data sets used for the gold dielectric function. Reproduced from **Paper II**.

dominates, SFG and SHG present the same behaviour. At 20500 cm^{-1}, the second interband transition starts to be excited, which is a common feature for both SFG and SHG curves. A deviation begins around 27000 cm^{-1}, where the first interband transition is passed for the incoming SFG frequency. SFG presents a resonance coinciding with the second interband transition band-edge, then a general decrease in the SFG intensity is present due to the oxygen adsorption. The SHG response does not manifest additional discrete features, only a progressive change which goes from a strong decrease of intensity at low frequencies but reverses this behaviour at high frequencies as the incoming light frequency reaches the second interband transition edge at 41000 cm^{-1}.

Below 27000 cm^{-1}, the bound electron contribution to the effective second order susceptibility is negligible. Above 27000 cm^{-1}, bound electrons have an increased contribution but the free electron one is still decisive, so the SFG resonance has a similar origin of the one at lower frequencies. Similarly, the sloping trend of the SHG response has a free electron contribution that gains a coupled bound-free electron contribution at the second interband transition edge, and the bound electron contribution remains at frequencies above that edge.

The lack of agreement between our calculated value of 461 nm with the literature value of 532 nm for the reverse behaviour could be due how the model considers the surface bound electron polarizability. In the model it is presumed that the polarizability remains at its bulk value, but this could be incorrect. Variation in the polarizability would have little effect on the low sum-frequency range since they do not influence the effective second order susceptibility, but they would have more noticeable effects at higher frequencies.

3.3 *In situ* investigation of electrochemically-formed gold oxide from gold films with X-ray spectroscopies

In **Paper III**, the different stages of gold oxide formation were investigated with both *operando* HERFD-XANES and *in situ* HP-XPS to expand upon the observations from the *ex situ* XPS and *operando* SFG in **Paper I**. Figure 3.8 (upper panel) shows *operando* HERFD-XANES spectra spectra of Au L_3 edge for metallic gold; oxidized gold at 1.38 V and 1.72 V vs. the reversible hydrogen electrode (RHE), and Au_2O_3 as reference. Electrochemical treatments were done in an acidic electrolyte ($HClO_4$, 1M), and the spectra collection started after a stable anodic current was observed. When gold turns from its metallic state into an oxidised one, its white line (around 11919 eV) acquires intensity and becomes sharper,[147–150] and this is seen in the upper panel in figure 3.8. As mentioned in section 2.1.3, the white line here is due to the transition from Au $2p_{3/2}$ to Au $5d_{5/2,3/2}$.

FEFF-computed HERFD-XANES spectra (in **Paper III** SI) for a metallic gold surface and Au_2O_3 are in good agreement with the experimental ones, while the computed spectrum of adsorbed OH groups on gold has a white line that does not match the experimental data. Hence, a linear fit calculation of the experimental spectra of gold metal and Au_2O_3 to the experimental HERFD-XANES spectra collected at 1.38 and 1.72 V vs. RHE was done, as shown in the lower panel of figure 3.8. The weights for 1.38 V are 0.87 and 0.13 for gold metal and Au_2O_3, respectively. For 1.72 V, the weights are 0.70 and 0.30 for gold metal and Au_2O_3, respectively. These results are in agreement with the expected increased contribution of gold oxide at higher electrochemical potentials. However, the component at 11933 eV is underestimated in the fit, while the component at 11946 eV is overestimated. These variations could be due to substantial contribution from the Au $5d$ – O $2p$ hybridized orbital at the white line resonance, leading to a higher intensity from the gold atom in the oxide than the metallic gold. Hence, the calculated weights from the linear fit underestimate the presence of gold oxide.

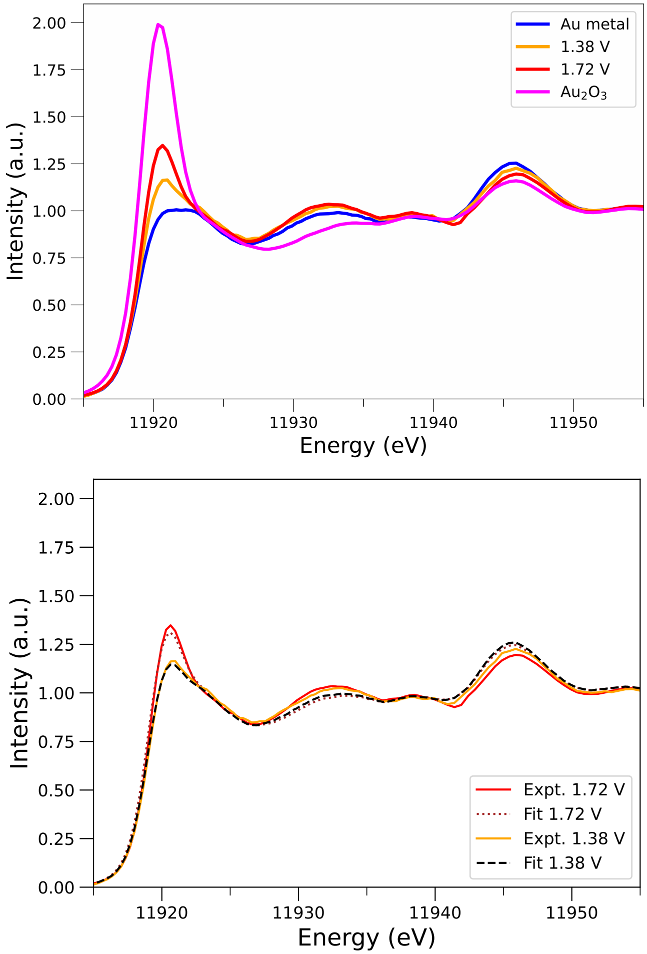

Figure 3.8: *Upper panel:* Experimental HERFD-XANES spectra collected *in situ* and *operando* during CA. The legend shows the investigated cases: gold metal surface, 1.38 and 1.72 V vs. RHE, while Au_2O_3 is a reference spectrum collected to facilitate the analysis. *Lower panel:* The experimental data collected at 1.38 and 1.72 V vs. RHE was fitted with the experimental metallic gold and Au_2O_3 spectra. Reproduced from **Paper III**.

A similar characterisation was done with *in-situ* HP-XPS with an incident photon energy of 7 keV and a background pressure of 30 mbar of water vapour to prevent the electrolyte from evaporating from the gold surface. Here, the electrochemical potential was applied until a stable current was reached while keeping the gold working electrode (WE) immersed in the electrolyte (H_3PO_4, 1M). Then, the oxidation process was stopped and the WE was lifted while keeping the bottom part in the electrolyte to form an electrolyte film on the surface (dip-and-pull method), and then the XPS spectra were collected. Figure 3.9 shows the Au $3d_{5/2}$ and O $1s$ spectra for the non-oxidised gold surface (upper panel), and for an oxidised gold surface after applying 2.56 V vs. RHE.

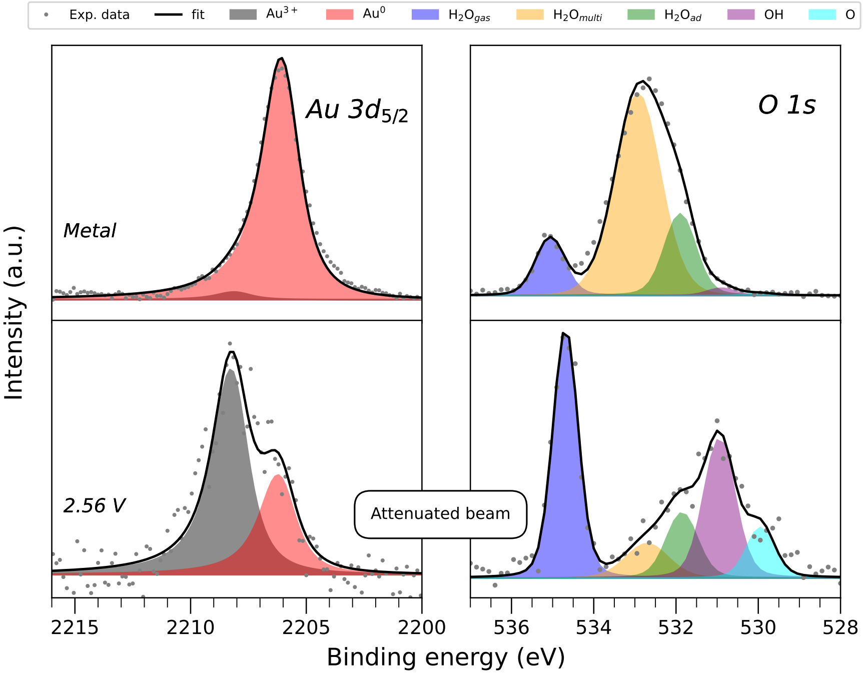

Figure 3.9: *In situ* HP-XPS spectra of Au $3d_{5/2}$ and O $1s$ core-levels before (top panels) and after (bottom panels) electrochemical oxidation at 2.56 V vs. RHE. All spectra were collected with 7 keV photons and in 30 mbar water vapor. Metal gold was measured with $f = 4.3 \cdot 10^6\, ph \cdot s^{-1} \cdot \mu m^{-2}$. The oxidized electrode was measured with higher X-ray beam attenuation ($f_{attenuated} = 1.4 \cdot 10^6\, ph \cdot s^{-1} \cdot \mu m^{-2}$) to reduce impact from bream induced oxide reduction. Reproduced from **Paper III**.

The Au $3d_{5/2}$ region presents a single peak for metallic gold (Au^0, 2206.1 eV) before oxidation, while after applying 2.56 V a new component at 2208.2 eV is observed due to Au^{3+} species. Similarly, the O $1s$ region (right side of figure 3.9) shows contributions due to oxidation after applying 2.56 V, which are OH and O on the Au surface at 531.0 and 529.5 eV, respectively; other than multi-layered and adsorbed water (H_2O_{multi} and H_2O_{ad}, 533 – 531 eV).[53;92;139] The new components in the O 1s-region due to oxidation are mainly assigned to gold (hydr-)oxides with a potential minor contribution of surface chemisorbed OH (OH_{ad}) and O (O_{ad}).

High photon fluxes could cause beam induced changes which can affect the data acquisition process. Spectra for *in situ* prepared samples need to be collected in a short time to verify the presence of beam induced effects, since in our case gold oxide is only continuously formed during *operando* HERFD-XANES characterisation. The XPS Au 3$d_{5/2}$ region was chosen for the beam damage study because it is recorded significantly faster than the HERFD-XANES Au L_3 edge. Figure 3.10 shows the time evolution of Au 3$d_{5/2}$ for an oxidised gold surface during the exposure of two different photon fluxes: $f_8 = 4.3 \cdot 10^6$ ph·s^{-1}·μ m^{-2} and $f_{25} = 1.4 \cdot 10^6$ ph·s^{-1}·μ m^{-2}. The beamline settings were kept the same. In both cases, the Au^{3+} component is reduced and at the same time the metallic component grows, even if the overall exposure time is within the time interval of gold oxide stability,[151] suggesting that the reduction of the oxide is promoted by X-ray beam induced effects. A similar effect was not observed during the *operando* HERFD-XANES measurements, even if the flux was higher than the one for *in situ* HP-HAXPES measurements. This indicates that working in *operando* conditions – in our case, continuously oxidising the electrode – helps to prevent a net reduction. This study shows the importance of developing *operando* HP-XPS methods to allow the study of low-Z elements in reactants, reaction intermediates, and products, which are difficult to obtain by XANES methods.

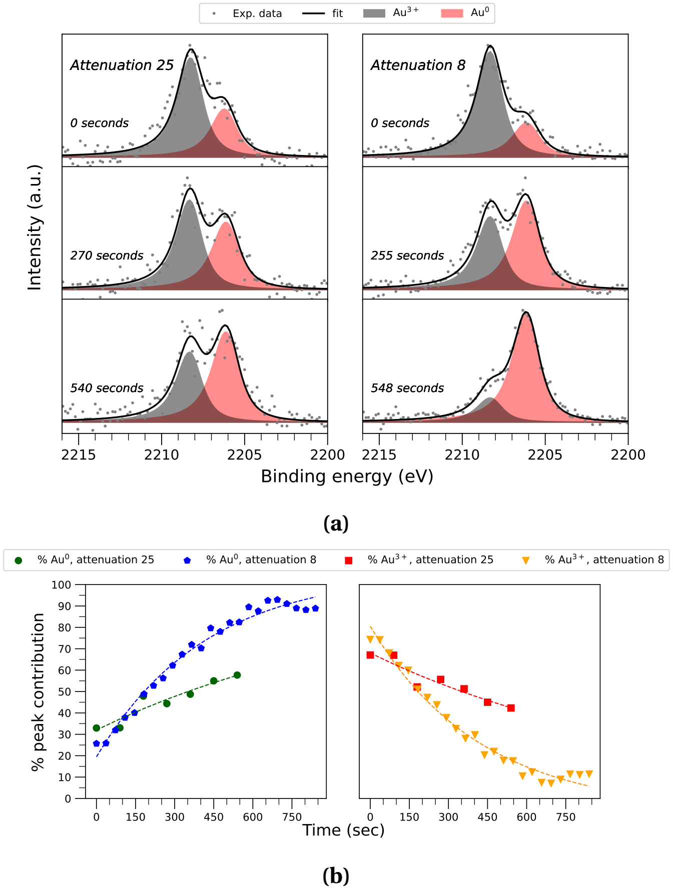

(a)

(b)

Figure 3.10: HP-XPS beam induced reduction study using two different X-ray beam fluxes $f_{att.25} = 1.4 \cdot 10^6\ ph \cdot s^{-1} \cdot \mu m^{-2}$ (left) and $f_{att.8} = 4.3 \cdot 10^6\ ph \cdot s^{-1} \cdot \mu m^{-2}$ (right) in 30 mbar water vapor using a photon energy of 7 keV. (a) XPS Au $3d_{5/2}$ core-level region at recorded at different X-ray exposure times. (b) Compression of the time evolution of the beam induced oxide reduction. The curves represent the relative integrated intensity for (left) metallic gold and (right) gold oxide.

3.4 Catalytic studies of low-temperature CO oxidation on Au-Fe_2O_3 and Au-TiO_2

While the previous sections focused on gold nanofilms, this last section of chapter 3 presents research on gold nanoparticles. Gold nanoparticles supported on metal oxides are used to catalyse low-temperature CO oxidation, an important reaction to *e.g.* remove CO contamination from H_2 fuel for fuel cells. **Paper IV** aims to bring more clarity about the reaction steps involved in the CO oxidation catalysed by Au-Fe_2O_3 and Au-TiO_2 by combining MS and density functional theory (DFT).

Figure 3.11 shows CO oxidation tests performed at 25 °C on Au-γ-Fe_2O_3 and Au-TiO_2. In the presence of only CO (1 vol %) and H_2O (2.8 vol %) with balance N_2 in the inlet flow, Au-TiO_2 has an inert response (figure 3.11.a, blue circles), while Au-γ-Fe_2O_3 generates 0.95 mmol CO_2 (mol Au)$^{-1}$s^{-1} within the first hour, followed by a rapid decrease in activity (figure 3.11.b, blue circles) because (in the absence of O_2) the support is slowly drained of oxygen. The possibility of H_2 production was tested but not detected, ruling out that the water gas shift reaction is involved in CO_2 production. Since Au-TiO_2 does not participate in the CO oxidation process, it seems in line with the previously proposed Langmuir-Hinshelwood (LH) mechanism where a product is formed from adsorbed reactants on the catalyst surface. However, Au-γ-Fe_2O_3 has a different behaviour with respect to what was previously reported, which can be classified as lattice Mars-van-Krevelen (MvK) mechanism, meaning a product is formed from one or more constituents from the support.

When O_2 (20 vol %) is also included in the inlet flow (figure 3.11, orange squares), the rates of both catalysts are in agreement with literature.[152;153] For Au-γ-Fe_2O_3, the maximum rate without O_2 (0.95 mmol CO_2 (mol Au)$^{-1}$s^{-1}) is ≈13 % of the maximum rate with O_2, but in the presence of O_2 this rate might be higher due to the continuous loading of lattice-oxygen.

DFT is used to verify the feasibility of the reaction steps for the observed water-promoted CO_2 production through a w-MvK mechanism. Figure 3.12 depicts the suggested w-MvK mechanism in the presence of Au-γ-Fe_2O_3. In reaction 15 (R15), CO is adsorbed on gold nanoparticle. In R16, CO adsorbed on the gold nanoparticle interaction with a oxygen from γ-Fe_2O_3 to produce CO_2, with an estimated activation energy of 0.98 eV.

When water is included, a low-barrier lattice-mediated scheme is available (R17 – R19). R17 is a dissociative absorption of H_2O onto an Fe_{lat}–O_{lat} motif in the γ-Fe_2O_3 surface where water is split into a hydroxyl on top of Fe_{lat}(OH_{ad}) and a lattice-hydroxyl (OH_{lat}). In R18, the CO adsorbed on gold reacts with the water-derived OH_{ad}, in this way a carboxylic group (COOH) is formed on the Au nanoparticle. In R19, this carboxylic group reacts with the OH_{lat} formed in R17 to produce CO_2 and form H_2O, creating a lattice oxygen

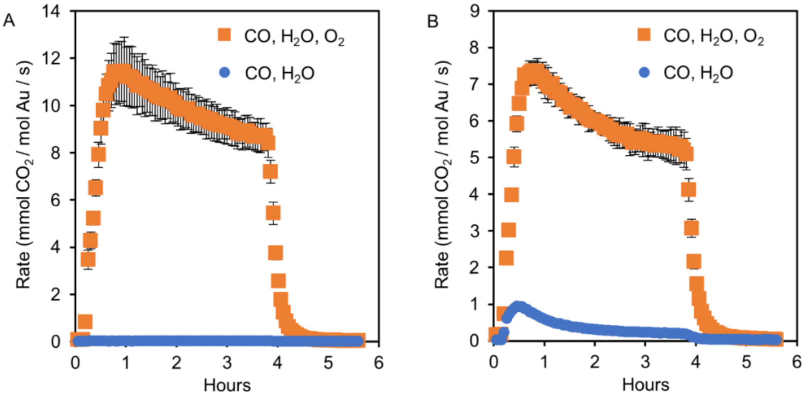

Figure 3.11: (A) Transient CO oxidation rates over Au-TiO_2. (B) Transient CO oxidation rates over Au-γ-Fe_2O_3. Reaction starts immediately upon introduction of CO, and terminates immediately upon removal of CO (at 3 h 45 min). Orange squares: 1 vol % CO, 2.8 vol % H_2O, 20 vol % O_2, balance N_2. Blue circles: 1 vol % CO, 2.8 vol % H_2O, balance N_2. Reaction temperature was 25 °C, and pressure 1 atm. Reported curves are averages of three independent measurements. Error bars are 2 standard deviations wide. Reproduced from **Paper IV**.

vacancy. In R17–19, there is no net consumption of water, since it is first consumed then formed again using oxygen from the γ-Fe_2O_3 lattice, hence R17–19 and R16 have the same stoichiometry. R18 has the highest barrier (0.44 V) in R17–19, which is lower than R16 (0.98 eV). In R20, an oxygen vacancy is filled with oxygen from O_2(g), depositing an oxygen atom (O^*) on the Au nanoparticle. In R21, the Au NP with O^* reacts with CO to form CO_2. Both R20 and R21 are almost without energy barriers.

The activation energies for both the LH paths suggested by Chandler and Iglesia have been calculated in this study.[66;154] They have the same rate determining step, that is O_2(g) activation by water to form OOH with activation energy of 0.55 eV. This means that both an LH mechanism and a w-MvK mechanism could be present at the same time when Au-γ-Fe_2O_3 is the catalyst with our previously-found result of at least 13 % CO_2 coming from a w-MvK mechanism.

Measurements of CO oxidation in the presence of $H_2{}^{18}O$ were conducted to further discriminate between the three considered mechanisms. Figure 3.13 shows transient CO oxidation experiments on Au-γ-Fe_2O_3 in the presence of $C^{16}O$, $^{16}O_2$ and $H_2^{18}O$ with conditions as 3.11. Figure 3.13.a depicts the transient production rates of $C^{16}O_2$, $C^{18}O^{16}O$, and $C^{18}O_2$. But, CO_2 also directly exchanges oxygen with $H_2{}^{18}O$ in the reactor piping and on the catalyst. This exchange in our reactor has been quantified for Chandler's and Iglesia's mechanisms, and for our w-MvK mechanism. Figure 3.13.b shows their transient relative abundances in the reactor effluent. In contrast with the

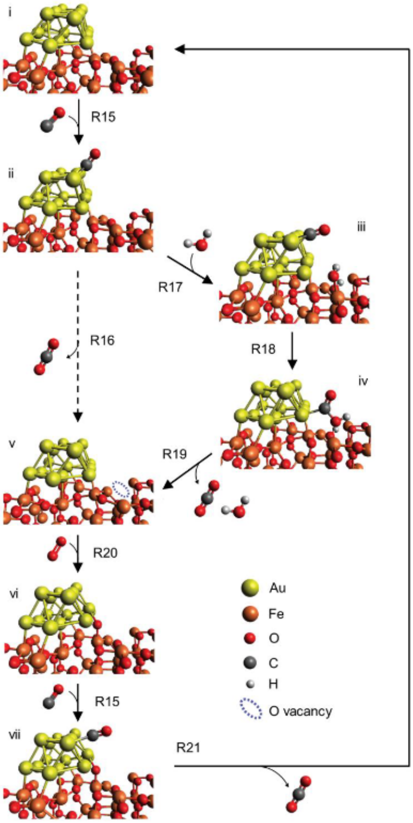

Figure 3.12: Schematic representation of our proposed mechanism for w-MvK CO oxidation (R15, R17 – R21) over Au-γ-Fe_2O_3. The non-feasible, non-water promoted, MvK mechanism is represented by R15, R16, R20, R21. Reproduced from **Paper IV**.

predicted abundances of Chandler's and Iglesia's reported LH mechanisms reported in figure 3.13.c, our suggested w-MvK mechanism is in agreement, within one percentage point, with the experimental data.

Gold nanoparticles supported on two different metal oxides were considered for catalysing CO oxidation: Au-TiO_2 behaved as previously suggested following a LH-mechanism at room temperature; Au-γ-Fe_2O_3, considering the results in figures 3.11 and 3.13, exhibited a lattice reaction, which can be described with our proposed w-MvK mechanism (figure 3.12).

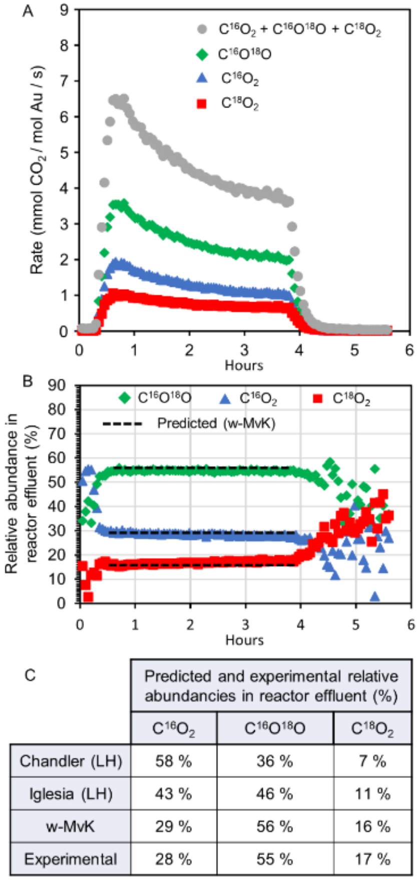

	Predicted and experimental relative abundancies in reactor effluent (%)		
	$C^{16}O_2$	$C^{16}O^{18}O$	$C^{18}O_2$
Chandler (LH)	58 %	36 %	7 %
Iglesia (LH)	43 %	46 %	11 %
w-MvK	29 %	56 %	16 %
Experimental	28 %	55 %	17 %

Figure 3.13: $C^{16}O$ oxidation over Au-γ-Fe_2O_3 with $H_2^{18}O$ and $^{16}O_2$. (A) Transient production rates of different isotopic CO_2 – species, and the total rate. (B) Transient relative abundances of different isotopic CO_2 – species in the reactor effluent. The relative abundances predicted from our proposed w–MvK mechanism are indicated by dashed lines. (C) Comparison between predicted (from different mechanistic hypotheses), and experimentally observed relative abundances in the reactor effluent. Reproduced from **Paper IV**.

4. Conclusions and Outlook

Gold-based materials have recently gained revalued interest for their catalytic properties at the nanoscale. However, full comprehension of the mechanistic processes underlying these properties is still lacking. In this thesis, three types of gold materials are investigated: electrochemically-formed gold oxide, electrochemically-formed oxide-derived gold, and gold nanoparticles supported on metal oxides.

Through a combined investigation using *operando* sum frequency generation (SFG) spectroscopy and *ex situ* high-pressure X-ray photoelectron spectroscopy (HP-XPS), subsurface gold oxide remnants were found to remain after electrochemical formation of oxide-derived gold from gold films, which might help explain its enhanced catalytic activity over pure metallic gold. The SFG signal variation together with elctorchemical gold oxidation processes were further studied using mathematical models. These models provide some insight about the origin of the SFG oxidation response, which seems to be due to changes of the free surface electron density by adsorbed oxygen. In addition, they suggest that the oxide forms from small islands that are centres for 3D oxide growth.

Further, *in situ* HP-XPS and *operando* high energy resolution fluorescence detected X-ray absorption near edge structure (HERFD-XANES) spectroscopies were employed, adding information about the changes in chemical composition of gold after electrochemical treatments. In addition, these two methods were compared with respect to beam induced effects, showing that *operando* conditions are needed to maintain a stable oxidised sample during measurements.

Gold nanoparticles supported on metal oxides (γ-Fe_2O_3 and TiO_2) were studied to understand the catalytic mechanism of CO oxidation to CO_2 on their surface. This research was performed using mass spectrometry measurements. This study suggests that different reaction mechanisms happen between the two different samples: a water-promoted Mars-van-Krevelen reaction on γ-Fe_2O_3, and a Langmuir-Hinshelwood reaction on TiO_2.

This work sets the basis for future studies of gold-based materials. It would be interesting to investigate the electrochemical behaviour of OD-Au formed at different pH values to get a better understanding of formation of subsurface oxide remnants, and to verify their possible role in CO_2 reduction to CO. In addition, different gold nanoparticles sizes and metal oxide supports could be tested to better elucidate the reaction steps and find more efficient catalysts for CO oxidation to CO_2.

Populärvetenskaplig sammanfattning

Denna avhandling omfattar fyra elektrokemiska och katalytiska studier av olika guldytor. En introduktion av de experimentella teknikerna föregår diskussion av resultaten från studierna.

I **Artikel I** undersöks oxidhärlett guld (OD-Au), som framställts elektrokemiskt under sura förhållanden (1M H_3PO_4, pH 1), med *operando* optisk summafrekvensgenerering (SFG) och *ex situ* röntgenfotoelektronspektroskopi vid högt tryck (HP-XPS), varvid det påvisas förekomsten av guldoxidrester (som Au_2O_3 eller $Au(OH)_3$) under det översta guldlagret av OD-Au. För att bättre förklara SFG-data genomförs ytterligare undersökningar av bildning av guldoxid under sura förhållanden och tillhörande förändring i elektronstrukturen genom matematisk modellering kombinerad med experimentella mätningar i **Artikel II**. Dessutom, för att bättre förstå den kemiska sammansättningen av guldoxiderna som bildas under oxidation samt strålningsinducerade effekter på provet, användss *in situ* HP-XPS och *operando* högupplöst fluorescensdetektion kombinerat med nära bandkantröntgenabsorption (HERFD-XANES) i **Artikel III**.

I **Artikel IV** görs experimentella studier av katalytisk oxidation av CO på Au-γ-Fe_2O_3 och Au-TiO_2 vid låga temperaturer. Masspektrometri används och olika syreisotoper (^{16}O och ^{18}O) används för att särskilja reaktionsstegen för CO och H_2O. Denna studie tyder på att vattenmedierad CO-oxidation på Au-γ-Fe_2O_3 sker via en Mars-van-Krevelenreaktion, vilket innebär att produkterna har en eller flera beståndsdelar från stödoxiden och vatten. På Au-TiO_2 däremot förlöper CO-oxidationen via en Langmuir-Hinshelwoodmekanism, vilket innebär att reaktionen istället sker mellan intilliggande adsorberade reaktionsintermediärer på ytan av katalysatorn.

Acknowledgements

My PhD journey has been like a roller coaster of self-questioning, success, and stressful periods. The closure of this path has been possible thanks to the people surrounding me. First, I would like to thank my PhD supervisor Prof. Tony Hansson for giving me the opportunity to start this journey so I could grow as a researcher. Your constant guidance during all these years has helped me finally reach the finish line. Secondly, I would like to thank my co-supervisor Dr. Sergey Koroidov for your critical thoughts and long constructive discussions. I would like to thank Dr. Markus Soldemo and Dr. Fernando Garcia-Martinez; I have learnt a lot working with you at the beamline and during the writing process of our articles. I would also like to thank the other lab-colleagues Dr. Christopher M. Goodwin, Dr. Ahmed El-Zohry, Dr. Vladimir Grigorev, Dr. David Degerman, Bernadette Davies, Dr. Alexander Holm, Dr. Patrick Lömker, and all the other co-authors; it has been a pleasure working with all of you.

I would like to thank Dr. Taras Golod for preparing the gold sample depositions, Dr. Mathias Hudl Waltin and my other co-supervisor Dr. Henrik Öström for helping with the laser maintenance. In addition, I would like to thank the technical division and the workshop at the Physics Department for their help with the lab setup.

Special thanks to my office mates and work-neighbours throughout the years: Kess M., Jesper N., Michael C., Berna A., Axel E., Gaia C., Tej V. Y., Lorenzo R., Sambit D., Deependra J., Eric D., Jonatan Ö., Roger C., Marjorie L. P., Maddalena B., Anita G., Sharon B., and Aigerim K. and the rest of the Chemical Physics division for the lunches, barbeques, fikor and fun times outside the workplace! And thanks to Crista A. W. who introduced me to pub quizzes, I really had fun with them and am looking forward to the next one!

Vorrei inoltre ringraziare la mia famiglia, in particolare i miei genitori, il vostro amore e supporto hanno accorciato le distanze dandomi la forza per andare avanti! Il vostro continuo spronarmi mi ha fatto raggiungere questo ulteriore traguardo. Cody il tuo amore incondizionato ha creato un accogliente rifugio su cui posso sempre contare. Questi anni insieme sono stati meravigliosi, non vedo l'ora di vedere cosa ci riserverà il futuro. In fine, vorrei ringraziare me stessa per aver osato intraprendere questo viaggio il quale mi ha portata ad esplorare il mondo!

References

[1] S. Boscolo Bibi. *Study of polycrystalline gold surfaces by potential-dependent optical sum frequency generation.* Licentiate thesis, Stockholm University, Stockholm, June 2022. v

[2] M. Berzelius. **On a new force acting in the formation of organic compounds**. *Journal of the Franklin Institute*, **22**(5):331–334, November 1836. 1

[3] **catalyst**. M. Nič, J. Jirát, B. Košata, A. Jenkins, and A. McNaught, editors, *IUPAC Compendium of Chemical Terminology.* IUPAC, Research Triagle Park, NC, 2.1.0 edition, June 2009. 1

[4] **biocatalyst**. M. Nič, J. Jirát, B. Košata, A. Jenkins, and A. McNaught, editors, *IUPAC Compendium of Chemical Terminology.* IUPAC, Research Triagle Park, NC, 2.1.0 edition, June 2009. 1

[5] *Horizons in sustainable industrial chemistry and catalysis.* Elsevier, Waltham, MA, 1st edition edition, 2019. 1

[6] H. Jahangiri, J. Bennett, P. Mahjoubi, K. Wilson, and S. Gu. **A review of advanced catalyst development for Fischer–Tropsch synthesis of hydrocarbons from biomass derived syn-gas**. *Catalysis Science and Technology*, **4**(8):2210–2229, 2014. 1

[7] J. Sá and J. Szlachetko. **Heterogeneous Catalysis Experiments at XFELs. Are we Close to Producing a Catalysis Movie?** *Catalysis Letters*, **144**(2):197–203, February 2014. 1

[8] Compiled by A. D. McNaught and A. Wilkinson. *IUPAC. Compendium of Chemical Terminology, 2nd ed. (the "Gold Book").* Blackwell Scientific Publications, Oxford, 1997. 2

[9] S. P. Davies. *Catalysis by Gold.* PhD thesis, Cardiff University, 2017. 2

[10] S. Srivaths. *Study of adsorption of methanol in an activated carbon and carbon nanotube matrix for use in a solar based refrigeration cycle.* PhD thesis, Texas A&M University, 2011. 2

[11] K. Marks. *Experimental investigations of model catalytic surface reactions on metals and metal-oxide surfaces.* PhD thesis, Stockholm University, 2019. 3, 25

[12] A. Delcourt Lancon. *Electrochemical analysis supported by macro and microelectrode array.* PhD thesis, Durham University, 2011. 3, 31

[13] *Misconceptions in Chemistry.* Springer Berlin Heidelberg, Berlin, Heidelberg, 2009. 3

[14] A. J. Bard and L. R. Faulkner. *Electrochemical methods: fundamentals and applications.* Wiley, New York, 2nd ed edition, 2001. 3, 4, 29, 36

[15] W. Schmickler and E. Santos. *Interfacial Electrochemistry.* Springer Berlin Heidelberg, Berlin, Heidelberg, 2010. 3, 4

[16] M. M. Waegele, C. M. Gunathunge, J. Li, and X. Li. **How cations affect the electric double layer and the rates and selectivity of electrocatalytic processes**. *Journal of Chemical Physics*, **151**(16):160902, October 2019. 4

[17] B. B. Damaskin and O. A. Petrii. **Historical development of theories of the electrochemical double layer**. *Journal of Solid State Electrochemistry*, **15**(7-8):1317–1334, July 2011. 4

[18] F. Scholz. **Voltammetric techniques of analysis: the essentials**. *ChemTexts*, **1**(4):17, December 2015. 4, 5

[19] G. Zwaschka, F. Lapointe, R. Kramer Campen, and Y. Tong. **Characterization of ultrafast processes at metal/solution interfaces: Towards femtoelectrochemistry**. *Current Opinion in Electrochemistry*, **29**:100813, October 2021. 5, 6

[20] L. D'Amario, M. B. Stella, T. Edvinsson, M. Persico, J. Messinger, and H. Dau. **Towards time resolved characterization of electrochemical reactions: electrochemically-induced Raman spectroscopy**. *Chemical Science*, **13**(36):10734–10742, 2022. 5

[21] C. M Gunathunge, J. Li, X. Li, and M. M. Waegele. **Surface-Adsorbed CO as an Infrared Probe of Electrocatalytic Interfaces**. *ACS Catalysis*, page 12, 2020. 6

[22] S. Wallentine, S. Bandaranayake, S. Biswas, and L. R. Baker. **Direct Observation of Carbon Dioxide Electroreduction on Gold: Site Blocking by the Stern Layer Controls CO_2 Adsorption Kinetics**. *Journal of Physical Chemistry Letters*, (11):8307–8313, 2020. 6

[23] B. Hammer and J. K. Norskov. **Why gold is the noblest of all the metals**. *Nature*, **376**(6537):238–240, July 1995. 7

[24] B. Hammer and J. K. Nørskov. **Theoretical surface science and catalysis—calculations and concepts**. *Advances in Catalysis*, **45**, pages 71–129. Elsevier, 2000. 7

[25] M. Che. **Nobel Prize in chemistry 1912 to Sabatier: Organic chemistry or catalysis?** *Catalysis Today*, **218-219**:162–171, December 2013. 7

[26] A. J. Medford, A. Vojvodic, J. S. Hummelshøj, J. Voss, F. Abild-Pedersen, F. Studt, T. Bligaard, A. Nilsson, and J. K. Nørskov. **From the Sabatier principle to a predictive theory of transition-metal heterogeneous catalysis**. *Journal of Catalysis*, **328**:36–42, August 2015. 8

[27] R. de Levie. **The electrolysis of water**. *Journal of Electroanalytical Chemistry*, (476):2, 1999. 8

[28] O. Diaz-Morales, F. Calle-Vallejo, C. de Munck, and M. T. M. Koper. **Electrochemical water splitting by gold: evidence for an oxide decomposition mechanism**. *Chemical Science*, **4**(6):2334–2343chen, 2013. 8

[29] S. Cherevko, A. A. Topalov, I. Katsounaros, and K. J.J. Mayrhofer. **Electrochemical dissolution of gold in acidic medium**. *Electrochemistry Communications*, **28**:44–46, March 2013. 8, 41

[30] M. Pourbaix. **Atlas of electrochemical equilibria in aqueous solutions**. *Journal of Electroanalytical Chemistry and Interfacial Electrochemistry*, **13**(4):471, April 1967. 8, 9

[31] N. P. Finkelstein and R. D. Hancock. **A new approach to the chemistry of gold**. *Gold Bull*, **7**(3):72–77, September 1974. 9

[32] M. Peuckert, F.P. Coenen, and H.P. Bonzel. **On the surface oxidation of a gold electrode in 1N H_2O_4 electrolyte**. *Surface Science Letters*, **141**(2-3):515–532, June 1984. 9, 42, 43

[33] K. Juodkazis, J. Juodkazyte, V. Jasulaitiene, A. Lukinskas, and B. Sebeka. **XPS studies on the gold oxide surface layer formation**. *Electrochemistry Communications*, **2**(7):503–507, July 2000. 42

[34] N. Weiher. *Combined in situ and ex situ studies of an electrochemical interface: investigation of anodic oxide layers on gold.* PhD thesis, Freie Universitaet, Berlin, 2003. 9

[35] S. J. Xia and V. I. Birss. **A multi-technique study of compact and hydrous Au oxide growth in 0.1 M sulfuric acid solutions**. *Journal of Electroanalytical Chemistry*, **500**(1-2):562–573, March 2001. 9, 10, 39, 41, 43, 45

[36] M. T. M. Koper. **Theory of multiple proton–electron transfer reactions and its implications for electrocatalysis**. *Chememical Science*, **4**(7):2710–2723, 2013. 10, 43

[37] S. YANG AND D. G. H. HETTERSCHEID. **Redefinition of the Active Species and the Mechanism of the Oxygen Evolution Reaction on Gold Oxide**. *ACS Catalysis*, **10**(21):12582–12589, November 2020. 10

[38] L. D. BURKE AND P. F. NUGENT. **The electrochemistry of gold: I the redox behaviour of the metal in aqueous media**. *Gold Bull*, **30**(2):43–53, June 1997. 10, 39

[39] J. PEREZ, E. R. GONZALEZ, AND H. M. VILLULLAS. **Hydrogen Evolution Reaction on Gold Single-Crystal Electrodes in Acid Solutions**. *Journal Physical Chemistry B*, **102**(52):10931–10935, December 1998. 10

[40] A. GOYAL, G. MARCANDALLI, V. A. MINTS, AND M. T. M. KOPER. **Competition between CO_2 Reduction and Hydrogen Evolution on a Gold Electrode under Well-Defined Mass Transport Conditions**. *Journal of American Chemical Society*, **142**(9):4154–4161, March 2020. 10

[41] M. TIAN, W. G. PELL, AND B. E. CONWAY. **Nanogravimetry study of the initial stages of anodic surface oxide film growth at Au in aqueous $HClO_4$ and H_2SO_4 by means of EQCN**. *Electrochimica Acta*, **48**(18):2675–2689, August 2003. 10, 46

[42] B. E. CONWAY, B. BARNETT, H. ANGERSTEIN-KOZLOWSKA, AND B. V. TILAK. **A surface-electrochemical basis for the direct logarithmic growth law for initial stages of extension of anodic oxide films formed at noble metals**. *The Journal of Chemical Physics*, **93**(11):8361–8373, December 1990. 10, 11

[43] G. TREMILIOSI-FILHO, L.H. DALL'ANTONIA, AND G. JERKIEWICZ. **Growth of surface oxides on gold electrodes under well-defined potential, time and temperature conditions**. *Journal of Electroanalytical Chemistry*, **578**(1):1–8, April 2005. 11

[44] T. HAYASHI, K. TANAKA, AND M. HARUTA. **Selective Vapor-Phase Epoxidation of Propylene over Au/TiO2Catalysts in the Presence of Oxygen and Hydrogen**. *Journal of Catalysis*, **178**(2):566–575, September 1998. 11

[45] R. MEYER, C. LEMIRE, S. K. SHAIKHUTDINOV, AND H. J. FREUND. **Surface chemistry of catalysis by gold**. *Gold Bull*, **37**(1-2):72–124, March 2004.

[46] J. A. VAN BOKHOVEN. **Catalysis by Gold: Why Size Matters**. *Chimia*, **63**(5):257, May 2009.

[47] B. N. ZOPE, D. D. HIBBITTS, M. NEUROCK, AND R. J. DAVIS. **Reactivity of the Gold/Water Interface During Selective Oxidation Catalysis**. *Science*, **330**(6000):74–78, October 2010.

[48] Y. Y. WU, N. A. MASHAYEKHI, AND H. H. KUNG. **Au–metal oxide support interface as catalytic active sites**. *Catalysis Science and Technology*, **3**(11):2881, 2013.

[49] P. RODRIGUEZ AND M. T. M. KOPER. **Electrocatalysis on gold**. *Physical Chemistry Chemcal Physics*, **16**(27):13583–13594, 2014. 11

[50] M. HARUTA, N. YAMADA, T. KOBAJASHI, AND S. IIJIMA. **Gold catalysts prepared by coprecipitation for low-temperature oxidation of hydrogen and of carbon monoxide**. *Journal of Catalysis*, **115**(2):301–309, February 1989. 11

[51] Y. ZHOU, Z. WANG, AND C. LIU. **Perspective on CO oxidation over Pd-based catalysts**. *Catalysis Science and Technology*, **5**(1):69–81, 2015. 12

[52] E. DUCK PARK AND J. SUNG LEE. **Effects of Pretreatment Conditions on CO Oxidation over Supported Au Catalysts**. *Journal of Catalysis*, **186**(1):1–11, August 1999. 12

[53] A. I. STADNICHENKO, S. V. KOSHCHEEV, AND A. I. BORONIN. **Oxidation of the polycrystalline gold foil surface and XPS study of oxygen states in oxide layers**. *Moscow Univ. Chem. Bull.*, **62**(6):343–349, December 2007. 43, 52

[54] C. BÜRGEL, N. M. REILLY, G. E. JOHNSON, R. MITRIĆ, M. L. KIMBLE, A. W. CASTLEMAN, AND V. BONAČIĆ-KOUTECKÝ. **Influence of Charge State on the Mechanism of CO Oxidation on Gold Clusters**. *Journal of American Chemical Society*, **130**(5):1694–1698, February 2008. 12

[55] M. MA, B. J. TRZEŚNIEWSKI, J. XIE, AND W. A. SMITH. **Selective and Efficient Reduction of Carbon Dioxide to Carbon Monoxide on Oxide-Derived Nanostructured Silver Electrocatalysts**. *Angewandte Chemie Int. Ed.*, **55**(33):9748–9752, August 2016. 12

[56] H. KIM, H. SEO PARK, Y. JEONG HWANG, AND B. KOUN MIN. **Surface-Morphology-Dependent Electrolyte Effects on Gold-Catalyzed Electrochemical CO $_2$ Reduction**. *Journal of Physical Chemistry C*, **121**(41):22637–22643, October 2017.

[57] J. E. PANDER, D. REN, Y. HUANG, N. WEI XIAN LOO, S. HUI LEE HONG, AND B. SIANG YEO. **Understanding the Heterogeneous Electrocatalytic Reduction of Carbon Dioxide on Oxide-Derived Catalysts**. *ChemElectroChem*, **5**(2):219–237, January 2018. 12

[58] N. J. FIRET, M. A. BLOMMAERT, T. BURDYNY, A. VENUGOPAL, D. BOHRA, A. LONGO, AND W. A. SMITH. ***Operando* EXAFS study reveals presence of oxygen in oxide-derived silver catalysts for electrochemical CO$_2$ reduction**. *Journal of Materials Chemistry A*, **7**(6):2597–2607, 2019. 12

[59] Y. HORI, A. MURATA, K. KIKUCHI, AND S. SUZUKI. **ElectrochemicalReduction of Carbon Dioxide to Carbon Monoxide at a Gold Electrode in Aqueous Potassium Hydrogen Carbonate**. *Journal American Chemical Society, Chem Commun.*, pages 728–729, 1987. 12

[60] Y. HORI. **Electrochemical CO$_2$ Reduction on Metal Electrodes**. In CONSTANTINOS G. VAYENAS, RALPH E. WHITE, AND MARIA E. GAMBOA-ALDECO, editors, *Modern Aspects of Electrochemistry*, **42**, pages 89–189. Springer New York, 2008. Series Title: Modern Aspects of Electrochemistry. 12

[61] Y. CHEN, C. W. LI, AND M. W. KANAN. **Aqueous CO$_2$ Reduction at Very Low Overpotential on Oxide-Derived Au Nanoparticles**. *Journal of American Chemical Society*, **134**:19969–19972, 2012. 12

[62] Z. QI, J. BIENER, AND M. BIENER. **Surface Oxide-Derived Nanoporous Gold Catalysts for Electrochemical CO$_2$ -to-CO Reduction**. *ACS Applied Energy Materials*, **2**(11):7717–7721, November 2019. 12

[63] X. MIN, Y. CHEN, AND M. W. KANAN. **Alkaline O$_2$ reduction on oxide-derived Au: high activity and 4e$^-$ selectivity without (100) facets**. *Physical Chemistry Chemical Physics*, **16**(27):13601–13604, 2014. 12

[64] J. JUPILLE AND G. THORNTON, editors. *Defects at Oxide Surfaces*, **58** of *Springer Series in Surface Sciences*. Springer International Publishing, Cham, 2015. 12

[65] J. LIU, I. A. W. FILOT, Y. SU, B. ZIJLSTRA, AND E. J. M. HENSEN. **Optimum Particle Size for Gold-Catalyzed CO Oxidation**. *Journal of Physical Chemistry C*, **122**(15):8327–8340, April 2018. 13

[66] M. OJEDA, B. ZHAN, AND . IGLESIA. **Mechanistic interpretation of CO oxidation turnover rates on supported Au clusters**. *Journal of Catalysis*, **285**(1):92–102, January 2012. 13, 55

[67] R. W BOYD. *Nonlinear optics*. Academic Press, Burlington, Mass, 2008. OCLC: 890559758. 15

[68] C.P. VINOD. **Insights into Heterogeneous Catalysis through Surface Science Techniques**. In *New and Future Developments in Catalysis*, pages 289–304. Elsevier, 2013. 15

[69] Y. R. SHEN, X. D. ZHU, AND H. SUHR. **Surface vibrational spectroscopy by infrared-visible sum frequency generation**. *Physical Review B*, **35**(3047(R)), 1987. 16

[70] Y. R. SHEN. *Fundamentals of Sum-Frequency Spectroscopy*. Cambridge University Press, Cambridge, 2016. 16

[71] P. GUYOT-SIONNEST, J. H. HUNT, AND Y. R. SHEN. **Sum-frequency vibrational spectroscopy of a Langmuir film: Study of molecular orientation of a two-dimensional system**. *Physical Review Letters*, **59**(14):1597–1600, October 1987. 16

[72] A. MORITA AND J. T. HYNES. **A Theoretical Analysis of the Sum Frequency Generation Spectrum of the Water Surface. II. Time-Dependent Approach**. *Journal of Physical Chemistry B*, **106**(3):673–685, January 2002.

[73] J. A. McGuire and Y. R. Shen. **Ultrafast Vibrational Dynamics at Water Interfaces**. *Science*, **313**(5795):1945–1948, September 2006. 16

[74] H. Arnolds and M. Bonn. **Ultrafast surface vibrational dynamics**. *Surface Science Reports*, **65**(2):45–66, February 2010. 16, 17, 25

[75] A. D. Curtis, S. R. Burt, A. R. Calchera, and J. E. Patterson. **Limitations in the Analysis of Vibrational Sum-Frequency Spectra Arising from the Nonresonant Contribution**. *The Journal of Physical Chemistry C*, page 10, 2011. 17

[76] A. G. Lambert, P. B. Davies, and D. J. Neivandt. **Implementing the Theory of Sum Frequency Generation Vibrational Spectroscopy: A Tutorial Review**. *Applied Spectroscopy Reviews*, **40**(2):103–145, May 2005. 17, 18

[77] B. S. Mendoza, W. L. Mochan, and J. A. Maytorena. **Visible-infrared sum and difference frequency generation at adsorbate-covered Au**. 17, 45

[78] L. Dalstein, A. Revel, C. Humbert, and B. Busson. **Nonlinear optical response of a gold surface in the visible range: A study by two-color sum-frequency generation spectroscopy. I. Experimental determination**. *The Journal of Chemical Physics*, **148**(13):134701, April 2018. 17, 45

[79] B. Busson and L. Dalstein. **Nonlinear optical response of a gold surface in the visible range: A study by two-color sum-frequency generation spectroscopy. II. Model for metal nonlinear susceptibility**. *The Journal of Chemical Physics*, **149**(3):034701, July 2018. 17, 45

[80] B. Busson and L. Dalstein. **Sum-Frequency Spectroscopy Amplified by Plasmonics: The Small Particle Case**. *Journal of Physical Chemistry C*, **123**:27, 2019. 17

[81] M. J. Walters and D. Roy. **Interference of Linear and Nonlinear Optical Effects in Second-Harmonic Generation from Metal/Liquid Interfaces**. *Applied Spectroscopy*, **52**(12):1554–1568, December 1998. 17

[82] E. H. G. Backus, N. Garcia-Araez, M. Bonn, and H. J. Bakker. **On the Role of Fresnel Factors in Sum-Frequency Generation Spectroscopy of Metal–Water and Metal-Oxide–Water Interfaces**. *Journal of Physical Chemistry C*, **116**(44):23351–23361, November 2012. 18

[83] K. Niu and R. A. Marcus. **Sum frequency generation, calculation of absolute intensities, comparison with experiments, and two-field relaxation-based derivation**. *Proceedings of the National Academy of Sciences USA*, **117**(6):2805–2814, February 2020. 18

[84] C. Nordling, E. Sokolowski, and K. Siegbahn. **Precision Method for Obtaining Absolute Values of Atomic Binding Energies**. *Physical Review*, **105**(5):1676–1677, March 1957. 18

[85] A. Einstein. **Zur Elektrodynamik bewegter Körper**. *Annal of Physics*, **322**(10):891–921, 1905. 18

[86] D. A. Shirley. **High-Resolution X-Ray Photoemission Spectrum of the Valence Bands of Gold**. *Physical Review B*, **5**(12):4709–4714, June 1972. 20

[87] S. Tougaard. **Practical guide to the use of backgrounds in quantitative XPS**. *Journal of Vacuum Science & Technology A*, **39**(1):011201, 2021. 20

[88] G. H. Major, N. Fairley, P. M. A. Sherwood, M. R. Linford, J. Terry, V. Fernandez, and K. Artyushkova. **Practical guide for curve fitting in x-ray photoelectron spectroscopy**. *Journal of Vacuum Science & Technology A*, **38**(6):061203, December 2020. 20

[89] S. P. Chenakin and N. Kruse. **Au 4f spin–orbit coupling effects in supported gold nanoparticles**. *Physical Chemistry Chemical Physics*, **18**(33):22778–22782, 2016. 20

[90] M. Higo, Y. Matsubara, Y. Kobayashi, M. Mitsushio, T. Yoshidome, and S. Nakatake. **Formation and decomposition of gold oxides prepared by an oxygen-dc glow discharge from gold films and studied by X-ray photoelectron spectroscopy**. *Thin Solid Films*, **699**:137870, April 2020. 20

[91] A. S. SCHLACHTER AND F. J. WUILLEUMIER, editors. *New Directions in Research with Third-Generation Soft X-Ray Synchrotron Radiation Sources.* Springer Netherlands, Dordrecht, 1994. 20

[92] H. ALI-LÖYTTY, M. W. LOUIE, M. R. SINGH, L. LI, H. G. SANCHEZ CASALONGUE, H. OGASAWARA, E. J. CRUMLIN, Z. LIU, A. T. BELL, A. NILSSON, AND D. FRIEBEL. **Ambient-Pressure XPS Study of a Ni–Fe Electrocatalyst for the Oxygen Evolution Reaction**. *Journal of Physical Chemimitry C*, **120**(4):2247–2253, February 2016. 20, 43, 52

[93] M.B. TRZHASKOVSKAYA AND V.G. YARZHEMSKY. **Dirac–Fock photoionization parameters for HAXPES applications**. *Atomic Data and Nuclear Data Tables*, **119**:99–174, January 2018. 20, 21

[94] M.B. TRZHASKOVSKAYA AND V.G. YARZHEMSKY. **Dirac–Fock photoionization parameters for HAXPES applications, Part II: Inner atomic shells**. *Atomic Data and Nuclear Data Tables*, **129-130**:101280, September 2019. 20, 21

[95] H. FRICKE. **The K-Characteristic Absorption Frequencies for the Chemical Elements Magnesium to Chromium**. *Physical Review*, **16**(3):202–215, September 1920. 21

[96] J. STÖHR. *NEXAFS Spectroscopy*, **25** of *Springer Series in Surface Sciences.* Springer Berlin Heidelberg, Berlin, Heidelberg, 1992. 21, 22

[97] M. BAUER. **HERFD-XAS and valence-to-core-XES: new tools to push the limits in research with hard X-rays?** *Physical Chemistry Chemical Physics*, **16**(27):13827–13837, 2014. 23

[98] J. J. REHR, J. J. KAS, F. D. VILA, M. P. PRANGE, AND K. JORISSEN. **Parameter-free calculations of X-ray spectra with FEFF9**. *Physical Chemistry Chemical Physics*, **12**(21):5503, 2010. 23

[99] D. FRIEBEL, D. J. MILLER, D. NORDLUND, H. OGASAWARA, AND A. NILSSON. **Degradation of Bimetallic Model Electrocatalysts: An In Situ X-Ray Absorption Spectroscopy Study**. *Angewandte Chemie Int. Ed.*, **50**(43):10190–10192, October 2011. 23

[100] G. MA, D. LIU, AND H. C. ALLEN. **Vibrational broad bandwidth and scanning sum frequency generation spectroscopy of air-solid and air-liquid interfaces**. page 145, Denver, CO, October 2004. 23

[101] T. BRABEC, C. SPIELMANN, P. F. CURLEY, AND F. KRAUSZ. **Kerr lens mode locking**. *Optics Letters*, **17**(18):1292, September 1992. 23

[102] S. YEFET AND A. PE'ER. **A Review of Cavity Design for Kerr Lens Mode-Locked Solid-State Lasers**. *Applied Sciences*, **3**(4):694–724, December 2013. 23

[103] R. L. FORK, O. E. MARTINEZ, AND J. P. GORDON. **Negative dispersion using pairs of prisms**. *Optics Letters*, **9**(5):150, May 1984. 24

[104] F. L. PEDROTTI, L. S. PEDROTTI. *Introduction to optics.* 2018. OCLC: 1145279362. 24

[105] COHERENT INC. **Operator s Manual SDG Synchronization and Delay Generator**. 2005. 25

[106] LIGHT CONVERSION. *NDGF user's manual.* 2011. 25

[107] L. J. RICHTER, T. P. PETRALLI-MALLOW, AND J. C. STEPHENSON. **Vibrationally resolved sum-frequency generation with broad-bandwidth infrared pulses**. *Optics Letters*, **23**(20):1594, October 1998. 25

[108] J. ALS-NIELSEN AND D. MCMORROW. *Elements of modern X-ray physics.* Wiley, a John Wiley & Sons, Ltd Publication, Chichester, West Sussex, second edition, reprinted with revisions and corrections edition, 2017. 26

[109] **DESY, Machine Parameters PETRA III:** https://photon-science.desy.de/facilities/petra_iii/machine/parameters/index_eng.html. 27

[110] C Schlueter, A Gloskovskii, K Ederer, I Schostak, S Piec, I Sarkar, Y Matveyev, P Lömker, M Sing, R Claessen, C Wienmann, C Schneider, K Medjanik, G Schönhense, P Amann, A Nilsson, and W Drube. **The new dedicated HAXPES beamline P22 at PETRAIII**. *AIP Conference Proceedings*, **2054**:040010, 2019. 27

[111] **P22 Hard X-ray Photoelectron Spectroscopy:** https://photon-science.desy.de/facilities/petra_iii/beamlines/p22_haxpes/index_eng.html. 27

[112] P. Amann, D. Degerman, M. Lee, J. D. Alexander, M. Shipilin, H. Wang, F. Cavalca, M. Weston, J. Gladh, M. Blom, M. Björkhage, P. Löfgren, C. Schlueter, P. Loemker, K. Ederer, W. Drube, H. Noei, J. Zehetner, H. Wentzel, J. Åhlund, and A. Nilsson. **A high-pressure x-ray photoelectron spectroscopy instrument for studies of industrially relevant catalytic reactions at pressures of several bars**. *Review of Scientific Instruments*, **90**(10):103102, October 2019. 27

[113] B. Gilles. **Grazing incidence diffraction: A review**. pages 177–204, Frascati (Italy), 1996. 28

[114] W. A. Caliebe, V. Murzin, A. Kalinko, and M. Görlitz. **High-flux XAFS-beamline P64 at PETRA III**. *API Conference Proceedings*, 2054, 060031 (2019) 28

[115] **P64 - X-Ray Absorption Spectroscopy** https://photon-science.desy.de/facilities/petra_iii/beamlines/p64_advanced_xafs/unified_data_sheet/index_eng.html. 28

[116] A. Kalinko, W. A. Caliebe, R. Schoch, and M. Bauer. **A von Hamos-type hard X-ray spectrometer at the PETRA III beamline P64**. *Journal of Synchrotron Radiation*, **27**(1):31–36, January 2020. 28

[117] Metrohm. **Autolab Application Note EC03**. page 2. 29

[118] K.C. Honeychurch. **Printed thick-film biosensors**. In *Printed Films*, pages 366–409. Elsevier, 2012. 30

[119] B.E. Conway. **Electrochemical oxide film formation at noble metals as a surface-chemical process**. *Progress in Surface Science*, **49**(4):331–452, August 1995. 30

[120] A. Fattori. *Electrochemical and Spectroelectrochemical Studies of Dyes used in Dye-sensitized Solar Cells.* PhD thesis, 2010. 30

[121] N. Elgrishi, K. J. Rountree, B. D. McCarthy, E. S. Rountree, T. T. Eisenhart, and J. L. Dempsey. **A Practical Beginner's Guide to Cyclic Voltammetry**. *Journal of Chemical Education*, **95**(2):197–206, February 2018. 31

[122] T. Kuwana, R. K. Darlington, and D. W. Leedy. **Electrochemical Studies Using Conducting Glass Indicator Electrodes.** *Analytical Chemistry*, **36**(10):2023–2025, September 1964. 32

[123] W. Kaim and J. Fiedler. **Spectroelectrochemistry: the best of two worlds**. *Chemical Society Reviews*, **38**(12):3373, 2009. 32

[124] Y. Tong, F. Lapointe, M. Thämer, M. Wolf, and R. Kramer Campen. **Hydrophobic Water Probed Experimentally at the Gold Electrode/Aqueous Interface**. *Angewandte Chemie Int. Ed.*, **56**(15):4211–4214, April 2017. 32

[125] S. Axnanda, E. J. Crumlin, B. Mao, S. Rani, R. Chang, P. G. Karlsson, M. O. M. Edwards, M. Lundqvist, R. Moberg, P. Ross, Z. Hussain, and Z. Liu. **Using "Tender" X-ray Ambient Pressure X-Ray Photoelectron Spectroscopy as A Direct Probe of Solid-Liquid Interface**. *Scientific Reports*, **5**(1):9788, May 2015. 33

[126] J.C. Hoogvliet and W.P. van Bennekom. **Gold thin-film electrodes: an EQCM study of the influence of chromium and titanium adhesion layers on the response**. *Electrochimica Acta*, **47**(4):599–611, November 2001. 35

[127] M. H. Cheah and P. Chernev. **Electrochemical oxidation of ferricyanide**. *Scientific Reports*, **11**(1):23058, December 2021. 36

[128] P. GUYOT-SIONNEST AND A. TADJEDDINE. **Study of Ag(111) and Au(111) electrodes by optical second-harmonic generation**. *The Journal of Chemical Physics*, **92**(1):734–738, January 1990. 40, 46

[129] S. M.A. BATEN, A. G. TAYLOR, AND C. P. WILDE. **Second Harmonic Generation studies of the oxidation of metal electrodes: Compact and hydrous oxide growth at gold electrodes in acid solutions**. *Electrochimica Acta*, **53**(23):6829–6834, October 2008. 46

[130] I. NAHALKA, G. ZWASCHKA, R. KRAMER CAMPEN, A. MARCHIORO, AND S. ROKE. **Mapping Electrochemical Heterogeneity at Gold Surfaces: A Second Harmonic Imaging Study**. *Journal of Physical Chemistry C*, **124**(37):20021–20034, September 2020. 40, 46

[131] S. CHEREVKO, A. A. TOPALOV, A. R. ZERADJANIN, I. KATSOUNAROS, AND K. J. J. MAYRHOFER. **Gold dissolution: towards understanding of noble metal corrosion**. *RSC Advances*, **3**(37):16516, 2013. 41

[132] C. STUMM, S. GRAU, F. D. SPECK, F. HILPERT, V. BRIEGA-MARTOS, K. MAYRHOFER, S. CHEREVKO, O. BRUMMEL, AND J. LIBUDA. **Reduction of Oxide Layers on Au(111): The Interplay between Reduction Rate, Dissolution, and Restructuring**. *Journal of Physical Chemistry C*, **125**(41):22698–22704, October 2021. 41, 42

[133] T. DICKINSON, A. F. POVEY, AND P. M. A. SHERWOOD. **X-ray photoelectron spectroscopic studies of oxide films on platinum and gold electrodes**. *Journal of the Chemical Society, Faraday Transactions 1*, **71**(0):298, 1975. 42

[134] B. KOSLOWSKI, R. WAHRENBERG, AND P. OELHAFEN. **Oxidation of preferentially (111)-oriented Au films in an oxygen plasma investigated by scanning tunneling microscopy and photoelectron spectroscopy**. *Surface Science*, **475**:1–10, 2001.

[135] A. THOMPSON, I. LINDAU, D. ATTWOOD, Y. LIU, E. GULLIKSON, P. PIANETTA, M. HOWELLS, A. ROBINSON, K. KIM, J. SCOFIELD, J. KIRZ, J. UNDERWOOD, J. KORTRIGHT, G. WILLIAMS, AND H. WINICK. *X-ray data booklet.* Lawrence Berkley National Laboratory, University of California, Berkley, CA 94720, 2009.

[136] A. YU. KLYUSHIN, T. C. R. ROCHA, M. HÄVECKER, A. KNOP-GERICKE, AND R. SCHLÖGL. **A near ambient pressure XPS study of Au oxidation**. *Physical Chemistry Chemical Physics*, **16**(17):7881–7886, 2014.

[137] E. ARTMANN, L. FORSCHNER, K. M. SCHÜTTLER, M. AL-SHAKRAN, T. JACOB, AND A. K. ENGSTFELD. **Nanoporous Au Formation on Au Substrates via High Voltage Electrolysis****. *ChemPhysChem*, **24**(5):e202200645, 2023. 42

[138] P. M. A. SHERWOOD. **Introduction to Studies of Phosphorus-Oxygen Compounds by XPS**. *Surface Science Spectra*, **9**(1):62–66, December 2002. 43

[139] H. SANCHEZ CASALONGUE, S. KAYA, V. VISWANATHAN, D. J. MILLER, D. FRIEBEL, H. A. HANSEN, J. K. NØRSKOV, A. NILSSON, AND H. OGASAWARA. **Direct observation of the oxygenated species during oxygen reduction on a platinum fuel cell cathode**. *Nature Communications*, **4**(1):2817, December 2013. 43, 52

[140] S.L. MARSHALL AND B.E. CONWAY. **Analysis of molecular polarization and interaction in adsorbed monolayers at electrodes part 1. Interaction between adsorbed dipoles**. *Journal of Electroanalytical Chemistry*, **337**(1-2):1–18, October 1992. 45

[141] S. L. MARSHALL AND B. E. CONWAY. **Analysis of molecular polarization and interaction in adsorbed monolayers at electrodes Part 2. Surface solvation energy of adsorbed charges** *Journal of Electroanalytical Chemistry*, **337**(1-2):19–43, October 1992.

[142] S. L. MARSHALL AND B. E. CONWAY. **Analysis of molecular polarization and interaction in adsorbed monolayers at electrodes Part 4. Madelung constants for hexagonal lattices of adsorbed ions and dipoles**. *Journal of Electroanalytical Chemistry*, **337**(1-2):67–89, October 1992.

[143] S.L. MARSHALL AND B.E. CONWAY. **Analysis of molecular polarization and interaction in adsorbed monolayers of electrodes. Part 3. Ionic adsorption isotherm with mean field treatment of interactions involving ions and dipoles.** *Journal of Electroanalytical Chemistry*, **337**(1-2):45–66, October 1992. 45

[144] Y. FURUYA, T. MASHIO, A. OHMA, N. DALE, K. OSHIHARA, AND G. JERKIEWICZ. **Surface oxide growth on platinum electrode in aqueous trifluoromethanesulfonic acid**. *The Journal of Chemical Physics*, **141**(16):164705, October 2014. 45

[145] B. BUSSON AND L. DALSTEIN. **Nonlinear optical response of a gold surface in the visible range: A study by two-color sum-frequency generation spectroscopy. III. Simulations of the experimental SFG intensities**. *The Journal of Chemical Physics*, **149**(15):154701, October 2018. 45

[146] A. TADJEDDINE, W. Q. ZHENG, A. LE RILLE, O. PULCHERY, F. VIDAL, AND A. PEREMANS. **Sum and Difference Frequency Generation at the Electrochemical Interface**. *Physica Status Solidi A*, page 20, 1999. 46

[147] N. WEIHER, E. BUS, L. DELANNOY, C. LOUIS, D.E. RAMAKER, J.T. MILLER, AND J.A. VAN BOKHOVEN. **Structure and oxidation state of gold on different supports under various CO oxidation conditions**. *Journal of Catalysis*, **240**(2):100–107, June 2006. 49

[148] J. OHYAMA, K. TERAMURA, T. SHISHIDO, Y. HITOMI, K. KATO, H. TANIDA, T. URUGA, AND T. TANAKA. **In Situ Au L3 and L2 edge XANES spectral analysis during growth of thiol protected gold nanoparticles for the study on particle size dependent electronic properties**. *Chemical Physics Letters*, **507**(1-3):105–110, April 2011.

[149] S. CHANG, A. UEHARA, S. G. BOOTH, K. IGNATYEV, J. F. W. MOSSELMANS, R. A. W. DRYFE, AND S. L. M. SCHROEDER. **Structure and bonding in Au(I) chloride species: a critical examination of X-ray absorption spectroscopy (XAS) data**. *RSC Advances*, **5**(9):6912–6918, 2015.

[150] A. LONGO, F. GIANNICI, M. P. CASALETTO, M. ROVEZZI, C. J. SAHLE, P. GLATZEL, Y. JOLY, AND A. MARTORANA. **Dynamic Role of Gold *d*-Orbitals during CO Oxidation under Aerobic Conditions**. *ACS Catalysis*, **12**(6):3615–3627, March 2022. 49

[151] M. HIGO, M. MITSUSHIO, T. YOSHIDOME, AND S. NAKATAKE. **Characterization and preservation of gold oxides prepared by an oxygen-dc glow discharge from gold films and studied by X-ray photoelectron spectroscopy**. *Gold Bull*, **53**(2):77–92, June 2020. 52

[152] G. ŠMIT, N. STRUKAN, M. W.J. CRAJÉ, AND K. LÁZÁR. **A comparative study of CO adsorption and oxidation on Au/Fe_2O_3 catalysts by FT-IR and in situ DRIFTS spectroscopies**. *Journal of Molecular Catalysis A: Chemical*, **252**(1-2):163–170, June 2006. 54

[153] X. WEI, B. SHAO, Y. ZHOU, Y. LI, C. JIN, J. LIU, AND W. SHEN. **Geometrical Structure of the Gold–Iron(III) Oxide Interfacial Perimeter for CO Oxidation**. *Angewandte Chemie*, **130**(35):11459–11463, August 2018. 54

[154] J. SAAVEDRA, C. J. PURSELL, AND B. D. CHANDLER. **CO Oxidation Kinetics over Au/TiO_2 and Au/Al_2O_3 Catalysts: Evidence for a Common Water-Assisted Mechanism**. *Journal of American Chemical Society*, **140**(10):3712–3723, March 2018. 55